Available online at www.sciencedirect.com

ScienceDirect

Advances in Space Research 74 (2024) 3234–3255

ADVANCES IN SPACE RESEARCH (a COSPAR publication)

www.elsevier.com/locate/asr

Deep learning based fuzzy-MPC controller for satellite combined energy and attitude control system

Sohaib Aslam [a,b,*], Yew-Chung Chak [c], Mujtaba Hussain Jaffery [b], Renuganth Varatharajoo [c,d], Yury Razoumny [e]

[a] School of Information Technology, Deakin University, Burwood, VIC 3125, Australia
[b] Department of Electrical and Computer Engineering, COMSATS University Islamabad (CUI), Lahore Campus, Pakistan
[c] Department of Aerospace Engineering, Universiti Putra Malaysia, 4300 Serdang, Selangor, Malaysia
[d] Visiting Professor Group, Academy of Engineering, Peoples' Friendship University of Russia (RUDN University), Miklukho-Maklaya Str. 6, Moscow 117198, Russian Federation
[e] Department of Mechanics and Control, Academy of Engineering, Peoples' Friendship University of Russia (RUDN University), Miklukho-Maklaya Str. 6, Moscow 117198, Russian Federation

Received 14 March 2024; received in revised form 15 June 2024; accepted 12 July 2024
Available online 25 July 2024

Abstract

Combined Energy and Attitude Control System (CEACS) reduces the size and mass budgets of typical satellites and consequently, increases their payload capacity. CEACS uses flywheels for a dual purpose, i.e., as both energy storage and attitude control device. This maiden work attempts to introduce a novel Deep-Learning capability of the fuzzy-Model Predictive Control (FMPC) controller for CEACS. The design approach for the fuzzy-MPC controller uses the Takagi-Sugeno (T-S) fuzzy model of satellite attitudes and computes the control torque through a parallel distribution compensation (PDC) approach. However, the MPC controller offers a high computational burden, and it becomes a significant problem for smaller satellites having limited computational power. Therefore, in this research work, a novel Deep-Learning-based fuzzy-MPC controller (D-FMPC) is designed for the CEACS attitude regulation subject to higher initial angles, actuator constraints, parametric uncertainties, and external disturbance torques. Here, the deep-layer neural network is trained offline with the MPC controller data to replicate the FMPC controller, thus ensuring its controllability. Numerical results validate that the D-FMPC controller successfully mimics the FMPC controller and produces the desired pointing accuracy effectively with smooth transient response and without violating the attitude control actuator constraints. The results also validate that the D-FMPC controller offers significantly reduced computational burden than the FMPC controller. Therefore, the novel Deep-Learning solution provides a feasible platform for applying more complicated and sophisticated attitude control techniques for the CEACS attitude regulation in small satellites as an example.

Keywords: Attitude Control; CEACS; Constraints; Deep Learning; FMPC Control; Neural Network; Takagi-Sugeno fuzzy Model

1. Introduction

The use of small satellites for deep space missions has increased due to the number of advantages such as lower development and deployment cost, shorter development time, and better feasibility than conventional satellites to perform specific operations, i.e., in-situ measurement,

* Corresponding author at: School of Information Technology, Deakin University, Burwood, VIC 3125, Australia.
E-mail addresses: sohaib.aslam@deakin.edu.au (S. Aslam), samchak11@gmail.com (Y.-C. Chak), m.jaffery@cuilahore.edu.pk (M.H. Jaffery), renu99@gmx.de (R. Varatharajoo), yury.razoumny@gmail.com (Y. Razoumny).

https://doi.org/10.1016/j.asr.2024.07.034
0273-1177/

List of symbols

Ω_c	Angular speed issued by attitude controller
Ω_w	Actual angular speed
K_w	Proportional speed controller
k_m	Motor torque constant
T_w	Flywheel torque
I_w	Flywheel inertia
τ_w	Flywheel time constant
T_c	Commanded torque produced by the controller
Ω_v	Commanded angular speed to the flywheel
Ω_E	Angular speed governed by the energy control part
z_1, z_2	fuzzy variables
$\boldsymbol{x}(t)$	State vector
$\boldsymbol{u}(t)$	Input vector
$\mathbf{A}_i$	System matrix for ith T–S fuzzy rule
$\mathbf{B}_i$	Input matrix for ith T–S fuzzy rule
$\boldsymbol{y}(t)$	Output vector
$\mathbf{C}_i$	Output matrix
ρ	Input to the NN
W^m	Weight of layer m
σ^m	Activation function of hidden layer m
$\boldsymbol{\delta}$	A vector containing all biases and vectors
s	Laplace variable
$T_w(s)$	Flywheel torque in Laplace form
$\boldsymbol{x}(t)$	Continuous time state vector
$\dot{\boldsymbol{x}}$	Derivative of state vector
$\mathscr{F}_b$	Fixed body frame
ϕ	Roll angle
ψ	Yaw angle
N	Negative Membership function
ϕ_d, θ_d, ψ_d	Desired attitude angles
$\underline{N}_p$	Prediction horizon
$\mathbf{R}$	Cost matrix
$\Delta\boldsymbol{u}(k)$	Rate of change of control variable
$\mathbf{R}$	Correlation coefficient
$\alpha_i(t)$	Normalized weight for the ith fuzzy rule
$M_{ij}(z_j(t))$	Membership degree of fuzzy variable
ϕ, θ, ψ	Roll, Pitch and Yaw angles
$\omega_x, \omega_y, \omega_z$	Angular velocities
I_x, I_y, I_z	Principal moments of inertia
T_{wx}, T_{wy}, T_{wz}	Control torques about each axis of the satellite
T_{dx}, T_{dy}, T_{dz}	Disturbance torques along each axis
$\mathbf{A}_{di}$	Discrete-time system matrix
T_s	Sampling instant
$u_i^{\mathrm{MPC}}(k)$	Control signal generated by the MPC controller
T_c	Control torque governed by the FMPC/D-FMPC controller
N_p	Prediction horizon
N_c	Control horizon
$\mathbf{A}_g, \mathbf{B}_g, \mathbf{C}_g$	Augmented state-space matrices
M_k	Set of membership functions
R_s	Reference trajectory
α^m	Output of layer m
b^m	Biases of layer m
S^m	Number of neurons in layer m
$\boldsymbol{\eta}$	Vector containing Q error vectors
$T^{s/w}, T^{w/s}$	Projection matrices from satellite to flywheel and flywheel to satellite respectively
m_n^M	Set of membership functions
$\boldsymbol{y}(t)$	Output vector
$\mu_i(\boldsymbol{Z}(t))$	Product of functions $m_{ij}(z_j(t))$
$\mathscr{F}_I$	Fixed inertial frame
θ	Pitch angle
P	Positive membership function
e_x, e_y, e_z	Error signals
$\boldsymbol{u}(k)$	Control variable of MPC controller
$r(k)$	Set point
r_w	MPC tuning parameter
J	Cost function
N_c	Predicted control moves

larger satellites in-orbit inspection, earth observation constellation, and communication constellation. Therefore, the rapid development of these satellites has been recorded in recent years (He et al., 2021), and satellite engineers put great attention to mass and size optimization of a satellite along with ensuring a successful completion of satellite missions (Eshghi and Varatharajoo, 2017). One of the mass and size optimization approaches is to combine various satellite subsystems known as synergism. The two most crucial components within a satellite are the attitude control and power storage subsystems, and they together share a larger portion of the total mass of a satellite. The notion of merging these subsystems into a single entity was initially introduced for larger satellites in the 1960s but gained widespread recognition during the 1980s, coined as the Integrated Power and Attitude Control System (IPAC) (O'Dea et al., 1985; Flatley, 1985). Roithmayr used this integrated approach for the International Space Station (ISS) and provided an extensive report (Roithmayr, 1999). Similarly, this approach was evaluated in various studies and researchers observed significant performance enhancements. However, the investigations were predominantly focused on larger satellites (Richie et al., 2001; Yoon and Tsiotras, 2002; Tsiotras et al., 2001).

Varatharajoo applied this synergistic Combined Energy and Attitude Control System (CEACS) approach to the smaller satellites for the first time and examined it through a series of research works (Varatharajoo et al., 2011;

Varatharajoo, 2006a,b, 2004; Ban and Varatharajoo, 2013; Ban et al., 2012; Varatharajoo and Fasoulas, 2002). These studies provide comprehensive details on the complete system design of CEACS and its numerical validations. It is worthwhile to note that the energy storage function of CEACS has already been optimized and presented (Varatharajoo, 2006b). It is also important to note that that the CEACS attitude control and energy storage tasks are decoupled in their operation frequency domains. Over the last decade, the attitude-controlling perspective of CEACS has got remarkable attention from researchers and various linear and nonlinear control techniques have been evaluated (Ismail and Varatharajoo, 2020; Rouyan et al., 2019; Eshghi and Varatharajoo, 2017; Varatharajoo et al., 2011) and the primary focus of these investigations was to introduce an efficient control method for regulating CEACS attitude in the presence of environmental disturbance torques. The Proportional-Integral-Derivative (PID) controller was integrated with Active Force Control (AFC) to enhance CEACS attitude pointing accuracy. However, AFC needs in-situ measurements, which are not consistently accessible (Varatharajoo et al., 2011). Similarly, optimal controllers, i.e., H_2 and H_∞ have been used for CEACS attitude pointing accuracy enhancements (Ban and Varatharajoo, 2013; Ban et al., 2012); however, the small angle approximations used to simplify the satellite attitude model affect the accuracy of results in the aforesaid research. Therefore, Eshghi and Varatharajoo employed a nonlinear controller, i.e., Sliding Mode Control (SMC) technique to handle system nonlinearities and attain a satisfactory CEACS pointing precision (Eshghi and Varatharajoo, 2014). However, the onboard errors and high-frequency chattering problems degraded the attitude control performances. To eradicate this problem, Eshghi and Varatharajoo implemented a singularity-free integral augmented SMC controller (Eshghi and Varatharajoo, 2017).

fuzzy Logic Control (FLC) is one of the most famous controllers capable of handling nonlinearities and uncertainties of dynamic systems. Therefore, it has been widely used in aerospace applications (Chak and Varatharajoo, 2014; Giron-Sierra and Ortega, 2002; Ismail and Varatharajoo, 2020). Chak and Varatharajoo conducted an extensive investigation of the FLC controller's performance within the context of the synergistic approach known as the Combined Attitude and Sun Tracking System (CASTS). Their investigation included a spectrum of control strategies, ranging from the versatile fuzzy Proportional Derivative (PD) controller to the fuzzy gain scheduler, along with an adaptive fuzzy system aimed at mitigating external disturbance torques (Chak et al., 2021; Chak and Varatharajoo, 2017; Chak and Varatharajoo, 2015). In a separate study, Aslam et al. (2022) employed the fuzzy PD controller to improve the accuracy of attitude pointing in the CEACS while concurrently reducing the energy consumption of the actuators required to achieve the desired pointing accuracy. However, none of the previous works on CEACS addressed the issue of CEACS operational constraints. It is a well-known fact that the attitude actuators are capable of producing limited control torque and they may reach saturation due to attitude regulation with large initial angles or external disturbance torques consequently; however, it may end up with a satellite de-stabilization condition as well. Model Predictive Control (MPC) is a well-known optimal control technique for handling both input and output constraints systematically (Ashraf et al., 2020). However, performance of linear MPC controller gets degraded due to nonlinear dynamics of satellite, particularly at larger slew angles. Therefore, Aslam et al. (2023) designed the fuzzy MPC (FMPC) controller to achieve the desired satellite CEACS attitude pointing accuracy subject to actuator constraints, external disturbance torques, and larger initial angles. In this methodology, a non-linear system is transformed into several linear local subsystems by using the Takagi-Sugeno (T-S) fuzzy approach. Thus, subsequently, an MPC controller is individually tailored for each of these local subsystems. The final controller's output is attained by integrating the local outputs through a fuzzy-weighted scheme (Nova et al., 2022; Kuo and Resmi, 2019). T-S fuzzy modelling is a powerful tool to model a nonlinear system having various complexities, i.e., time delays, parametric uncertainties, faults, dead zone, saturation. Therefore, T-S fuzzy system provides a strong foundation for designing linear controllers for a highly nonlinear complex system (Wang et al., 2021).

The bottleneck in the MPC implementation for fast dynamic systems is its higher computational burden in comparison to the other linear controllers (Sarwar et al., 2019). This problem becomes significant in the FMPC controller design approach as multiple MPC controllers have been designed for the T-S fuzzy model of satellite attitudes and consequently it multiplies the overall computational burden. This limitation is critical for its implementation in smaller satellites due to their limited onboard computational power (George and Wilson, 2018). The problem that exists in already developed powerful processors used in computers and mobile phones is their vulnerability to space radiations and these cosmic radiations can interfere with the satellite computing operations. Therefore, expensive radiation-hardened processing devices for space missions are available but they offer extremely limited computational power.

Artificial Neural Networks (ANNs) exhibit an adaptive or learning nature, involving the adjustment of connection weights between interconnected processing units (neurons) in different layers. This tuning process aims to meet specific criteria set for the networks. Once the tuning is completed, either offline or online, the networks can effectively map the input and output relationship of a system, even without knowledge of its internal structure. The capability of learning complex patterns signifies the application of ANNs in satellite attitude control systems. In the literature, neural networks (NN) have been employed to

enhance satellite attitude pointing accuracy in various ways. Primarily, NNs serve two roles: firstly, as an estimator to determine uncertain parameters or functions, enhancing robustness and adaptability in attitude controllers; secondly, as an attitude controller approximator to replicate computationally intensive attitude controllers. Previous studies (Biggs and Fournier, 2019; Sivaprakash and Shanmugam, 2005; Kim et al., 2016) have utilized NNs to approximate the satellite's attitude controller. The use of NN to replicate computationally intensive optimal attitude control, employing four reaction thrusters for attitude regulation to minimize fuel consumption, has been explored in previous research (Biggs and Fournier, 2019). In this context, NN is trained offline using optimal data obtained from numerical simulations of the designed optimal controller. Additionally, NN has been applied to achieve three-axis stabilization for satellites using magnetic torquers in the presence of external disturbance torques and parametric uncertainty, as demonstrated by Sivaprakash and Shanmugam (2005). In this scenario, NN is trained using an input–output dataset obtained from simulated PD controllers for the satellite's attitude regulation problem. Similarly, the Neuro-fuzzy Controller (NFC) has been proposed for satellite attitude control with the aim of alleviating the high computational burden associated with the standard State-Dependent Riccati Equation (SDRE) controller (Kim et al., 2016). In this approach, a neuro-fuzzy inference system is trained offline using the dataset obtained from the simulated SDRE controller to approximate its behavior. The results demonstrate that the NFC controller not only outperforms the SDRE controller in the presence of parametric uncertainty but also exhibits a shorter execution time in computing the optimal control signal.

The objective of this work is to design a computationally efficient Deep Learning-based fuzzy MPC (D-FMPC) controller for regulating the attitude control of the CEACS with a desired pointing accuracy. This includes addressing challenges such as a nonlinear satellite, large initial angles, external disturbance torques, actuator constraints, and parametric uncertainty.

Here, the D-FMPC controller is designed in a two-step process. In the first step, FMPC controller is designed, capable of performing CEACS attitude regulation in the presence of external disturbance torques and CEACS actuator constraints. In the second step, the deep learning approach is used to train multilayer perception offline with the FMPC numerical data to replicate the computationally intensive attitude controller with the computationally efficient metamodel. It is important to note that the optimization of CEACS's energy storage function has been previously addressed and documented by Varatharajoo (2006a,b). Consequently, the D-FMPC controller has been exclusively designed and investigated for the purpose of regulating CEACS attitude.

The contributions of this research work are threefold as follows:

1. **Replica of FMPC Controller**: The first contribution of the proposed research is to design a deep learning based CEACS attitude controller that replicates the sophisticated fuzzy MPC controller, capable of performing the CEACS attitude regulation in the presence of higher initial angles, CEACS parametric uncertainty, and actuator constraints.
2. **Computationally Efficient Controller:** The second contribution is validating the computational efficiency of the proposed D-FMPC controller compared to the FMPC controller, making it viable for future space missions in general, and specifically for satellites with a limited computational power.
3. **Stability Demonstration:** The final contribution is to demonstrate the stability of the designed D-FMPC controller through Monte Carlo simulations as none of the previous works investigated the stability of a solely deep learning based attitude controller.

The structure of this paper is outlined as follows: Section 2 and Section 3 provide an explanation of the CEACS architecture, and the T-S fuzzy model employed for the rigid satellite. Section 4 provides the design details of FMPC and D-FMPC controllers. Section 5 presents the numerical findings of both controllers. Demonstrations of stability through Monte Carlo simulations are illustrated in Section 6. Finally, Section 7 concludes the paper and offers insights into future research directions.

2. CEACS architecture

The CEACS attitude control architecture employs a pair of high-speed counter-rotating flywheels mounted along the satellite axis. These flywheels are controllable in both speed and torque modes. However, speed mode is less sensitive to steady-state torque errors (Varatharajoo, 2006a) and it is used in this work as shown in Fig. 1.

where K_w, Ω_v, k_m, T_w, I_w, and Ω_w, represent speed control loop gain, desired angular speed, motor torque constant, flywheel torque, flywheel inertia, and actual angular speed. In this context, Ω_v represents the total speed, which is the sum of the speed set by the attitude controller (Ω_c) and the speed instructed by the energy control component (Ω_E) as shown in Eq. (1). The energy control component manages additional power generated by the solar panels, either by storing it in flywheels in the solar phase or acquiring it from them in the eclipse phase. The term $\frac{1}{I_w s}$ is a speed controller as it converts the torque into equivalent speed that governs the flywheel to achieve desired torque for satellite attitude regulation.

$$\Omega_v = \Omega_c + \Omega_E \tag{1}$$

The analytical relation between Ω_v and Ω_w for Fig. 1 is obtained after performing closed loop simplification

$$\Omega_w(s) = \left(\frac{1}{\frac{I_w}{K_w k_m}s + 1}\right)\Omega_v, \tag{2}$$

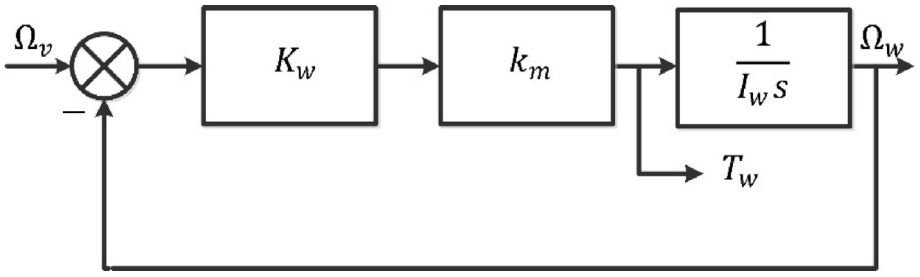

Fig. 1. Speed control mode of the flywheel.

Eq. (2) represents a first order delay, as given below

$$\Omega_w(s) = \left(\frac{1}{\tau_w s + 1}\right)\Omega_v, \tag{3}$$

where $\tau_w = \frac{I_w}{K_w k_m}$.

The analytical relation between the angular velocity and torque of a flywheel in the Laplace domain is given by

$$T_w(s) = I_w \Omega_w s. \tag{4}$$

By substituting the value of Ω_w from Eq. (4) in Eq. (3), the flywheel torque T_w becomes

$$T_w(s) = \left(\frac{1}{\tau_w s + 1}\right) I_w \Omega_v s. \tag{5}$$

Based on the counter-rotating flywheels configuration, the satellite attitude control through the CEACS mechanism is shown in Fig. 2. The net flywheel torque T_w at the output of CEACS is produced according to the desired control torque T_c requested by the attitude controller to achieve the desired attitude $\begin{bmatrix}\theta_{ref}\\ \dot{\theta}_{ref}\end{bmatrix}$. The CEACS torque T_w is realized by accelerating and decelerating the first and second flywheels respectively at specified required speeds. The resultant of this torque and the environmental disturbance torque T_d represented by T_s governs the satellite attitude. The measurements of satellite attitude $\begin{bmatrix}\theta\\ \dot{\theta}\end{bmatrix}$ are provided as feedback to the attitude controller. The CEACS architecture has been enclosed by a red dotted line in Fig. 2 and its analytical derivations have been presented in this section and the details about other blocks outside the dotted line are explained in the following subsections.

In Fig. 2, $T^{s/w}$ and $T^{w/s}$ are the projection matrices from the satellite to the flywheel and vice-versa. They are essential for transforming control signals and torques between the satellite's center of mass and flywheel's frame of reference. These transformations enable accurate control of the satellite's attitude by accounting for the physical locations

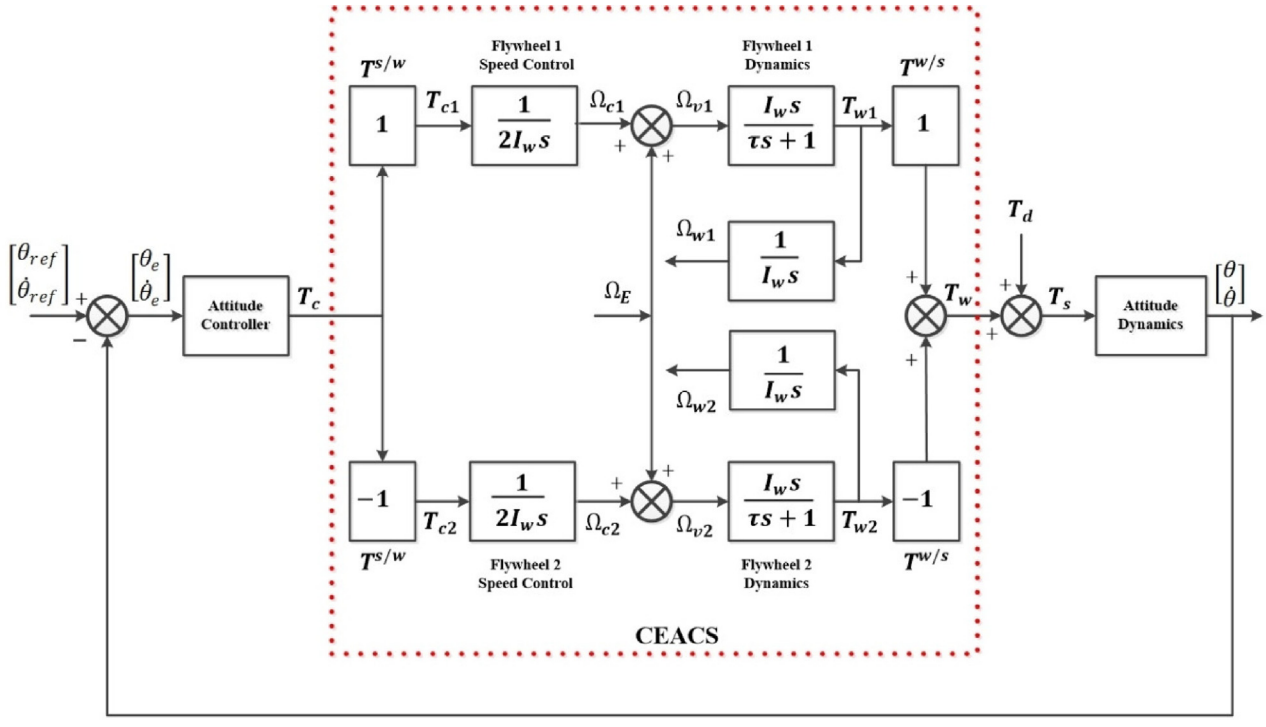

Fig. 2. CEACS architecture (Varatharajoo, 2004).

and orientations of the flywheels, ensuring the torques are correctly applied to the satellite's dynamics. For simplicity, it has been assumed that the torques produced by the flywheels are acting on the center of mass of the satellite, therefore, projection matrices have been assumed to be unity. Thus, according to projections, the control signals T_{c1} and T_{c2} are equal in magnitude to the control torque T_c but opposite in polarity as shown below

$$T_{c1} = T_c, \tag{6}$$

$$T_{c2} = -T_c. \tag{7}$$

Thus, both the flywheel speed controllers shown in Fig. 2 are governed by equal control torques with opposite polarity. Consequently, these control signals govern the speeds Ω_{c1} and Ω_{c2} for both flywheels

$$\Omega_{c1}(s) = \left(\frac{1}{2I_w s}\right) T_{c1}, \tag{8}$$

$$\Omega_{c2}(s) = \left(\frac{1}{2I_w s}\right) T_{c2}, \tag{9}$$

However, it is assumed that the counter-rotating flywheels must be alike in practice such that they possess the same inertia I_w.

The overall commanded speed for these flywheels is shown below

$$\Omega_{v1} = \Omega_{c1} + \Omega_E, \tag{10}$$

$$\Omega_{v2} = \Omega_{c2} + \Omega_E. \tag{11}$$

The torques produced by the counter-rotating flywheels are shown below

$$T_{w1}(s) = \left(\frac{I_w s}{\tau s + 1}\right) \Omega_{v1}, \tag{12}$$

$$T_{w2}(s) = \left(\frac{I_w s}{\tau s + 1}\right) \Omega_{v2}. \tag{13}$$

The resultant control torque produced by the CEACS configuration is calculated as

$$T_w(s) = T_{w1}(s) - T_{w2}(s), \tag{14}$$

A series of substitutions from Eqs. (8)–(13), modifies the Eq. (14) as follows

$$T_w(s) = \left(\frac{I_w s}{\tau s + 1}\right) \left[\frac{T_{c1}}{2I_w s} + \Omega_E - \left(\frac{T_{c2}}{2I_w s} + \Omega_E\right)\right], \tag{15}$$

Eq. (15) is further deduced to

$$T_w(s) = \left(\frac{1}{\tau s + 1}\right) \left[\frac{T_{c1} - T_{c2}}{2}\right], \tag{16}$$

Eq. (16) validates the operation of attitude control task is independent of the speed Ω_E requested by the energy control module.

From Eqs. (6) and (7), Eq. (16) can be simplified to

$$T_w(s) = \left(\frac{1}{\tau s + 1}\right) T_c. \tag{17}$$

This expression illustrates that the CEACS has the ability to generate the required torque, as seen in the case of a single flywheel, while also effectively handles the necessary energy management tasks concurrently.

3. Takagi–Sugeno fuzzy modelling of satellite attitude

T–S fuzzy model of satellite attitude is derived in this section.

3.1. Takagi–Sugeno fuzzy approach

In this approach, the if-then rules are used to characterize local linear dynamics of a nonlinear process in the form of a state space model, as given below (Chak and Varatharajoo, 2018).

$$\begin{aligned} R_i \;\; IF \;\; z_1(t) \;\; is \;\; m_1^K \wedge z_2(t) \;\; is \;\; m_2^L \wedge \cdots \wedge z_n(t) \;\; is \;\; m_n^M \\ \text{THEN} \;\; \dot{\boldsymbol{x}}^i = \mathbf{A}_i \boldsymbol{x} + \mathbf{B}_i \boldsymbol{u}, \qquad \boldsymbol{y}^i = \mathbf{C}_i \boldsymbol{x} \end{aligned} \tag{18}$$

where R_i represents the i^{th} rule within the set of R rules, $z_n(t)$ serves as the premise variable, and it can be a function of the continuous-time state vector $\boldsymbol{x}(t) \in \mathbb{R}^n$. Here, $\boldsymbol{u}(t) \in \mathbb{R}^m$ and $\boldsymbol{y}(t) \in \mathbb{R}^p$, and m_n^M represent the input vector, output vector, and set of membership functions respectively. Similarly, $\mathbf{A}_i \in \mathbb{R}^{n \times n}$, $\mathbf{B}_i \in \mathbb{R}^{n \times m}$, and $\mathbf{C}_i \in \mathbb{R}^{p \times n}$ represent system matrix, input matrix, output matrix respectively. Here, the consequent part of the rule represents the linear state-space model and is referred as subsystem. Following the defuzzification process, the entire fuzzy system's output is obtained

$$\begin{aligned} \dot{\boldsymbol{x}} &= \textstyle\sum_{i=1}^{n} \alpha_i(t) [\mathbf{A}_i \boldsymbol{x} + \mathbf{B}_i \boldsymbol{u}] \\ \boldsymbol{y} &= \textstyle\sum_{i=1}^{n} \alpha_i(t) \mathbf{C}_i \boldsymbol{x}, \end{aligned} \tag{19}$$

where

$$\alpha_i(t) = \frac{\mu_i(\boldsymbol{Z}(t))}{\sum_{i=1}^{n} \mu_i(\boldsymbol{Z}(t))}, \quad i = 1, 2, \cdots, n$$

$$\boldsymbol{z}(t) = [\, z_1(t) \quad z_2(t) \quad \cdots \quad z_n(t) \,],$$

$$\mu_i(\boldsymbol{Z}(t)) = \prod_{j=1}^{n} m_{ij}(z_j(t))$$

The term $m_{ij}(z_j(t))$ is the membership value of $z_j(t)$ for the membership function m_{ij}. The index i represents the rule number.

3.2. Satellite attitude fuzzy model

The satellite attitude model is represented by kinematic and dynamic equations of motion. The attitude kinematics of a satellite with a fixed body frame $\mathcal{F}_b$ relative to a fixed inertial frame $\mathcal{F}_I$ are represented in the ZYX Euler sequence as follows

$$\begin{bmatrix}\dot{\phi}\\ \dot{\theta}\\ \dot{\psi}\end{bmatrix}=\begin{bmatrix}1 & \mathrm{s}(\phi)\mathrm{t}(\theta) & \mathrm{c}(\phi)\mathrm{t}(\theta)\\ 0 & \mathrm{c}(\phi) & -\mathrm{s}(\phi)\\ 0 & \mathrm{s}(\phi)\mathrm{sc}(\theta) & \mathrm{c}(\phi)\mathrm{sc}(\theta)\end{bmatrix}\begin{bmatrix}\omega_x\\ \omega_y\\ \omega_z\end{bmatrix} \tag{20}$$

where $\{\phi,\theta,\psi\}$ is the set of Euler angles roll, pitch, and yaw respectively. Similarly, s, c, t, and sc represent *sin*, *cos*, *tan*, and *sec* respectively. The satellite's angular velocities with respect to the frame $\mathscr{F}_I$ are represented as $\{\omega_x,\omega_y,\omega_z\}$. Based on the Euler's angles and angular rates, the satellite's dynamic equations are given by

$$\begin{bmatrix}\dot{\omega}_x\\ \dot{\omega}_y\\ \dot{\omega}_z\end{bmatrix}=\begin{bmatrix}\left(\frac{I_y-I_z}{I_x}\right)\omega_y\omega_z\\ \left(\frac{I_z-I_x}{I_y}\right)\omega_z\omega_x\\ \left(\frac{I_x-I_y}{I_z}\right)\omega_x\omega_y\end{bmatrix}+\begin{bmatrix}\frac{T_{sx}}{I_x}\\ \frac{T_{sy}}{I_y}\\ \frac{T_z}{I_z}\end{bmatrix},$$
$$\begin{bmatrix}\dot{\omega}_x\\ \dot{\omega}_y\\ \dot{\omega}_z\end{bmatrix}=\begin{bmatrix}\left(\frac{I_y-I_z}{I_x}\right)\omega_y\omega_z\\ \left(\frac{I_z-I_x}{I_y}\right)\omega_z\omega_x\\ \left(\frac{I_x-I_y}{I_z}\right)\omega_x\omega_y\end{bmatrix}+\begin{bmatrix}\frac{T_{wx}+T_{dx}}{I_x}\\ \frac{T_{wy}+T_{dy}}{I_y}\\ \frac{T_{wz}+T_{dz}}{I_z}\end{bmatrix}, \tag{21}$$

where, $\{I_x,I_y,I_z\}$ are the principal moments of inertia, and $\{T_{sx},T_{sy},T_{sz}\}$ are the torques applied to the satellite. The satellite torques are the sum of the flywheel torques $\{T_{wx},T_{wy},T_{wz}\}$ produced by the CEACS actuation system for the satellite attitude regulation and the accumulative external disturbance torques $\{T_{dx},T_{dy},T_{dz}\}$ about each axis.

The research presented herein is well-suited for the task of stabilizing satellite attitude within an inertial space context, as might be the case with a space telescope. To achieve this, the differential attitude kinematic equations presented in Eq. (2) are simplified through the application of linearization approximations with reference to the $\mathscr{F}_I$ frame. Furthermore, a cuboid-shaped satellite with a symmetric inertia tensor $I_x=I_z$ is assumed which results in a systematic reduction in the required number of fuzzy rules to develop satellite's T-S fuzzy model. These simplifications collectively yield a quasilinear model for our investigation.

$$\begin{bmatrix}\dot{\phi}\\ \dot{\theta}\\ \dot{\psi}\\ \dot{\omega}_x\\ \dot{\omega}_y\\ \dot{\omega}_z\end{bmatrix}=\begin{bmatrix}0&0&0&1&0&0\\ 0&0&0&0&1&0\\ 0&0&0&0&0&1\\ 0&0&0&0&0&\left(\frac{I_y-I_z}{I_x}\right)\omega_y\\ 0&0&0&0&0&0\\ 0&0&0&0&\left(\frac{I_x-I_y}{I_z}\right)\omega_x&0\end{bmatrix}\begin{bmatrix}\phi\\ \theta\\ \psi\\ \omega_x\\ \omega_y\\ \omega_z\end{bmatrix}$$
$$+\begin{bmatrix}0&0&0\\ 0&0&0\\ 0&0&0\\ \frac{1}{I_x}&0&0\\ 0&\frac{1}{I_y}&0\\ 0&0&\frac{1}{I_z}\end{bmatrix}\begin{bmatrix}T_{wx}+T_{dx}\\ T_{wy}+T_{dy}\\ T_{wz}+T_{dz}\end{bmatrix}. \tag{22}$$

The first step towards implementation of T-S fuzzy model from Eq. (22) is the selection of fuzzy premise variables i.e., $z_1=-\left(\frac{I_y-I_z}{I_x}\right)\omega_y$ and $z_2=\left(\frac{I_x-I_y}{I_z}\right)\omega_x$. The next step is to assign fuzzy membership functions by calculating the minimum and maximum values of the fuzzy variables $[min(z_1),max(z_1)]$, and $[min(z_2),max(z_2)]$. For this purpose, the values of ω_x and ω_y are restricted within specified limits, i.e., $[min(\omega_x),max(\omega_x)]$ and $[min(\omega_y),max(\omega_y)]$. This approach is justified since the variables in physical systems are always confined within certain limits. Here, the universe of fuzzy variables comprises two triangular membership functions i.e., Negative (N) and Positive (P) and their membership values are calculated by

$$P(z_1)=\frac{z_1-min(z_1)}{max(z_1)-min(z_1)} \quad \& \quad N(z_1)=\frac{max(z_1)-z_1}{max(z_1)-min(z_1)} \tag{23}$$

$$P(z_2)=\frac{z_2-min(z_2)}{max(z_2)-min(z_2)} \quad \& \quad N(z_2)=\frac{max(z_2)-z_2}{max(z_2)-min(z_2)} \tag{24}$$

whereas minimum and maximum values of z_1 and z_2 are calculated by using the minimum and maximum values of ω_x and ω_y. Their membership plots are illustrated in Fig. 3.

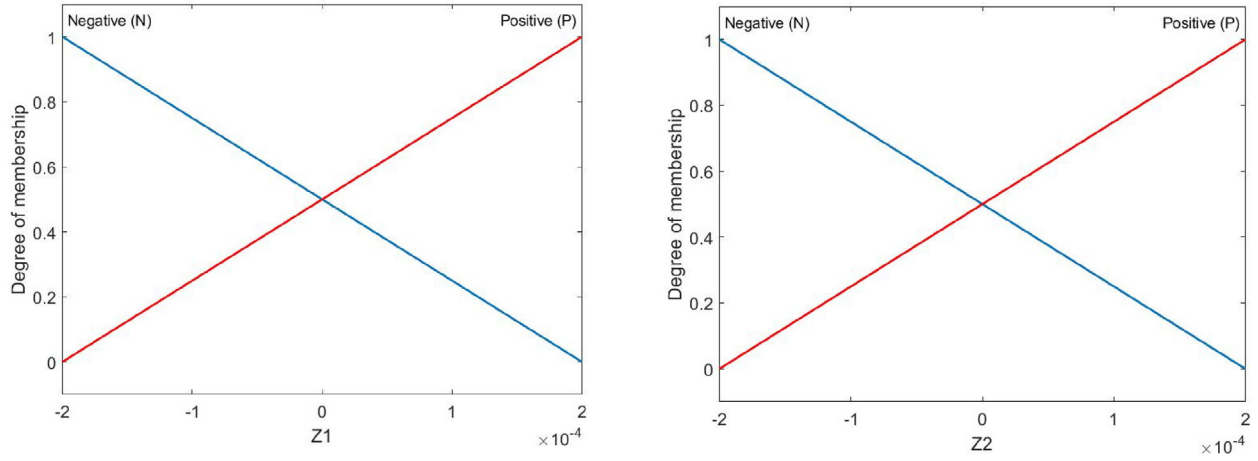

Fig. 3. Membership functions of fuzzy variables.

In this work, the controller's design relies on the discrete-time fuzzy model of the satellite. Therefore, the discrete-time fuzzy rules are given by

I. R_1 : If $z_1(k)$ *is P and* $z_2(k)$ *is P, Then*

$$\boldsymbol{x}_1(k+1) = \mathbf{A}_{1d}\boldsymbol{x}(\boldsymbol{k}) + \mathbf{B}\boldsymbol{u}(\boldsymbol{k}), \boldsymbol{y}(\boldsymbol{k}) = \mathbf{C}\boldsymbol{x}(\boldsymbol{k}) \tag{25}$$

II. R_2 : If $z_1(k)$ is P and $z_2(k)$ is N, Then

$$\boldsymbol{x}_2(k+1) = \mathbf{A}_{2d}\boldsymbol{x}(\boldsymbol{k}) + \mathbf{B}\boldsymbol{u}(\boldsymbol{k}), \boldsymbol{y}(\boldsymbol{k}) = \mathbf{C}\boldsymbol{x}(\boldsymbol{k}) \tag{26}$$

III. R_3 : If $z_1(k)$ is N and $z_2(k)$ is P, Then

$$\boldsymbol{x}_3(k+1) = \mathbf{A}_{3d}\boldsymbol{x}(\boldsymbol{k}) + \mathbf{B}\boldsymbol{u}(\boldsymbol{k}), \boldsymbol{y}(\boldsymbol{k}) = \mathbf{C}\boldsymbol{x}(\boldsymbol{k}) \tag{27}$$

IV. R_4 : If $z_1(k)$ is N and $z_2(k)$ is N, Then

$$\boldsymbol{x}_4(k+1) = \mathbf{A}_{4d}\boldsymbol{x}(\boldsymbol{k}) + \mathbf{B}\boldsymbol{u}(\boldsymbol{k}), \boldsymbol{y}(\boldsymbol{k}) = \mathbf{C}\boldsymbol{x}(\boldsymbol{k}) \tag{28}$$

Here, the fuzzy variables and membership functions are directly related in the system matrix i.e., N in fuzzy rule gives $min(z_i)$ and P gives $max(z_i)$ as shown below

$$\mathbf{A}_1 = \begin{bmatrix} 0 & 0 & 0 & 1 & 0 & 0 \\ 0 & 0 & 0 & 0 & 1 & 0 \\ 0 & 0 & 0 & 0 & 0 & 1 \\ 0 & 0 & 0 & 0 & 0 & -max(z_1(k)) \\ 0 & 0 & 0 & 0 & 0 & 0 \\ 0 & 0 & 0 & 0 & max(z_2(k)) & 0 \end{bmatrix},$$

$$\mathbf{A}_2 = \begin{bmatrix} 0 & 0 & 0 & 1 & 0 & 0 \\ 0 & 0 & 0 & 0 & 1 & 0 \\ 0 & 0 & 0 & 0 & 0 & 1 \\ 0 & 0 & 0 & 0 & 0 & -max(z_1(k)) \\ 0 & 0 & 0 & 0 & 0 & 0 \\ 0 & 0 & 0 & 0 & min(z_2(k)) & 0 \end{bmatrix},$$

$$\mathbf{A}_3 = \begin{bmatrix} 0 & 0 & 0 & 1 & 0 & 0 \\ 0 & 0 & 0 & 0 & 1 & 0 \\ 0 & 0 & 0 & 0 & 0 & 1 \\ 0 & 0 & 0 & 0 & 0 & -min(z_1(k)) \\ 0 & 0 & 0 & 0 & 0 & 0 \\ 0 & 0 & 0 & 0 & max(z_2(k)) & 0 \end{bmatrix}, \tag{29}$$

$$\mathbf{A}_4 = \begin{bmatrix} 0 & 0 & 0 & 1 & 0 & 0 \\ 0 & 0 & 0 & 0 & 1 & 0 \\ 0 & 0 & 0 & 0 & 0 & 1 \\ 0 & 0 & 0 & 0 & 0 & -min(z_1(k)) \\ 0 & 0 & 0 & 0 & 0 & 0 \\ 0 & 0 & 0 & 0 & min(z_2(k)) & 0 \end{bmatrix}.$$

The conversion from continuous time-matrices to discrete-time matrices is done through Zero Order Hold (ZOH) approach (Toth et al., 2008).

$$\mathbf{A}_{di} = e^{\mathbf{A}_i T_s}, \tag{30}$$

where T_s represents the discretization sampling interval. This discretized T-S fuzzy model corresponds to the continuous nonlinear system depicted in Eq. (22) over the interval $[min(\omega), max(\omega)]$.

4. Control design

The design approach of the D-FMPC controller includes three steps, the first step is the design of the FMPC controller for the satellite T-S fuzzy model. The second step includes the training of a deep-layer NN with the obtained meta data of the MPC controllers for each linear subsystem to replace the MPC controller with a computationally efficient controller. The final step is to compute a single control output from multiple NN-based trained controllers by using the parallel distribution compensation (PDC) approach.

4.1. FMPC controller design

The design of FMPC controller for the derived satellite's T-S fuzzy model is based on the PDC approach as presented below.

4.1.1. Parallel distribution compensation

The PDC approach is used here to design linear controllers for each subsystem by using T-S fuzzy framework, for a set of R rules it is given by

$$R_i \quad \text{IF } z_1(t) \text{ is } m_1^K \wedge z_2(t) \text{ is } m_2^L \wedge \cdots \wedge z_n(t) \text{ is } m_n^M \quad \text{THEN } \boldsymbol{u}_i^{\text{MPC}}(k), \tag{31}$$

where $\boldsymbol{u}_i^{\text{MPC}}(k)$ is the control vector governed by the MPC controller for the i^{th} T-S fuzzy rule. The global control vector is obtained after the defuzzification process (Aslam et al., 2023).

$$T_c = \sum_{i=1}^{R} \alpha_i(t) * u_i^{\text{MPC}}(k). \tag{32}$$

The FMPC implementation for the satellite CAECS attitude regulation is shown in Fig. 4. Here, $\{\phi_d, \theta_d, \psi_d\}$ represent desired attitude angles and $\{e_x, e_y, e_z\}$ represent the error signals.

4.1.2. MPC controller design

The MPC is a model-based control technique and here, the state-space-model is used in design of the controller. Consider a discrete-time LTI system

$$\begin{aligned} \boldsymbol{x}(k+1) &= \mathbf{A}\boldsymbol{x}(k) + \mathbf{B}\boldsymbol{u}(k), \\ \boldsymbol{y}(k) &= \mathbf{C}\boldsymbol{x}(k). \end{aligned} \tag{33}$$

The MPC controller performance is directly related to the perfection of the mathematical model, and any model-pant mismatch degrades the controller performance. To handle this issue, a velocity model is used (Wang, 2004; Sarwar

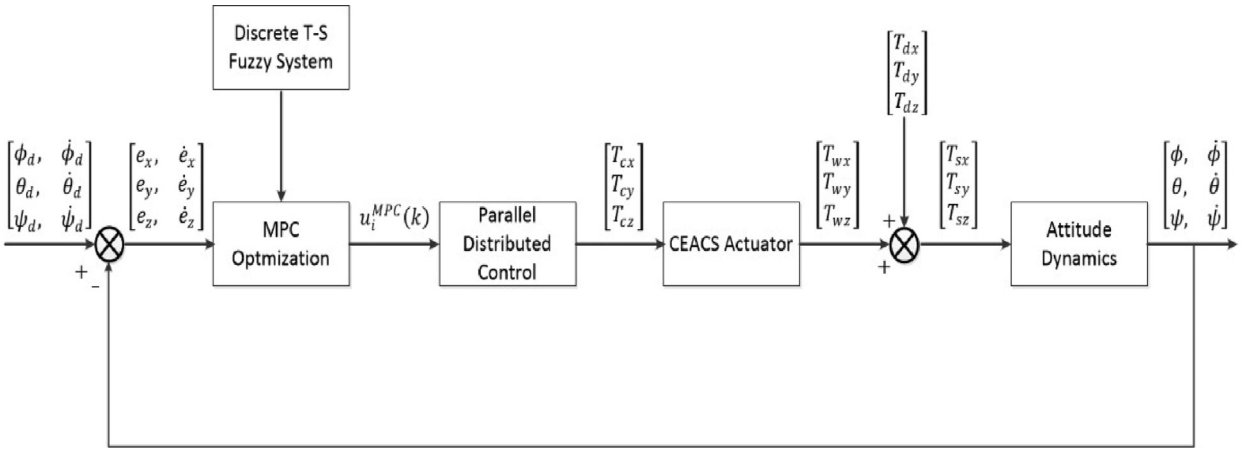

Fig. 4. FMPC controller for satellite CEACS.

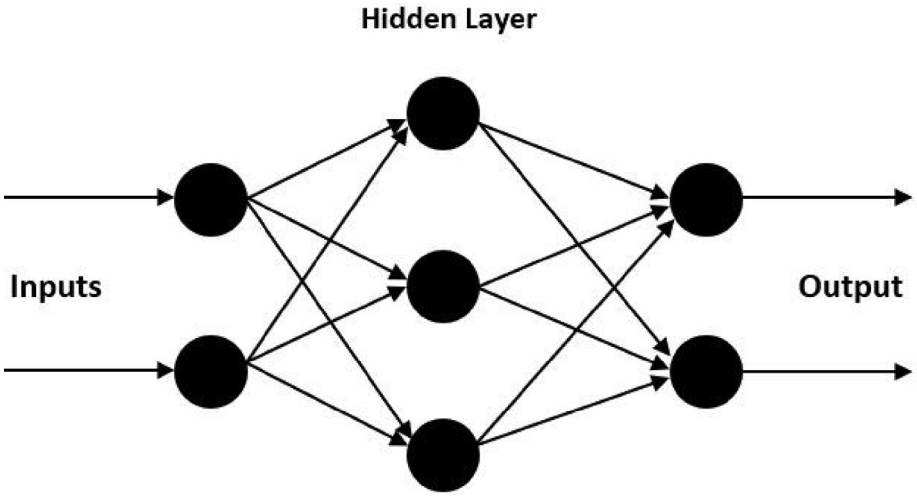

Fig. 5. Illustration of feedforward NN.

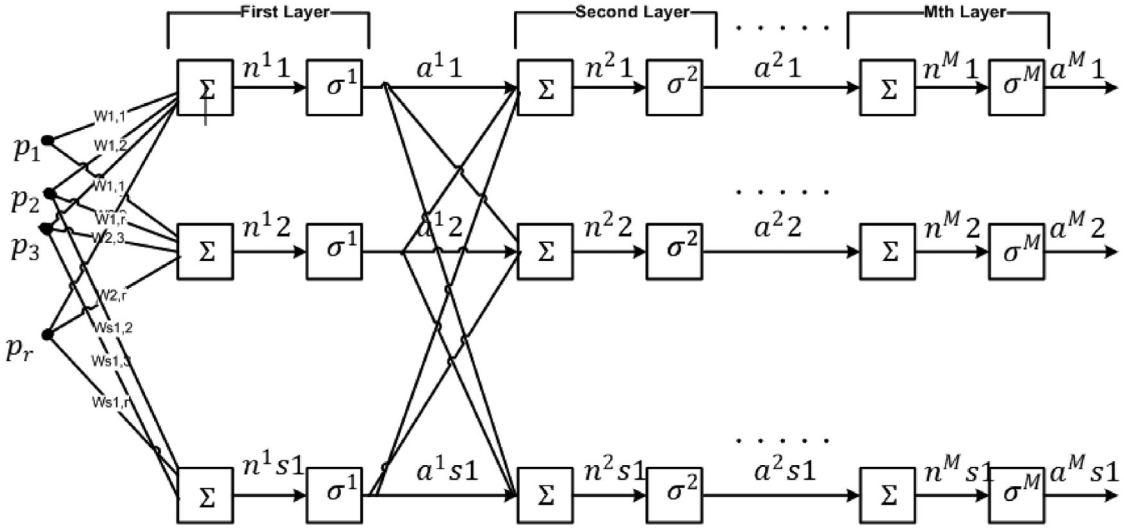

Fig. 6. Illustration of NN operation (Biggs and Fournier, 2019).

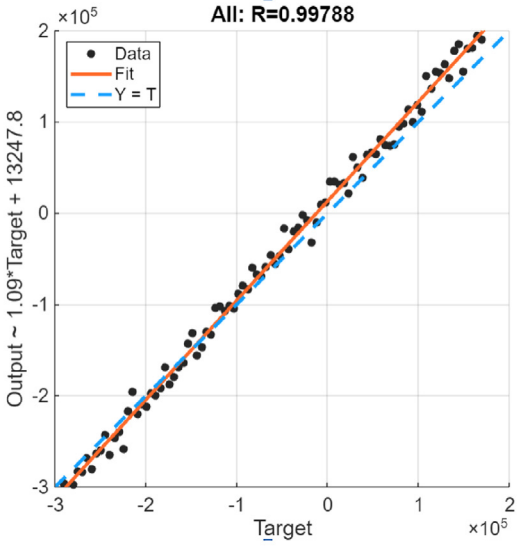

(a) Regression plot for MPC controller 1

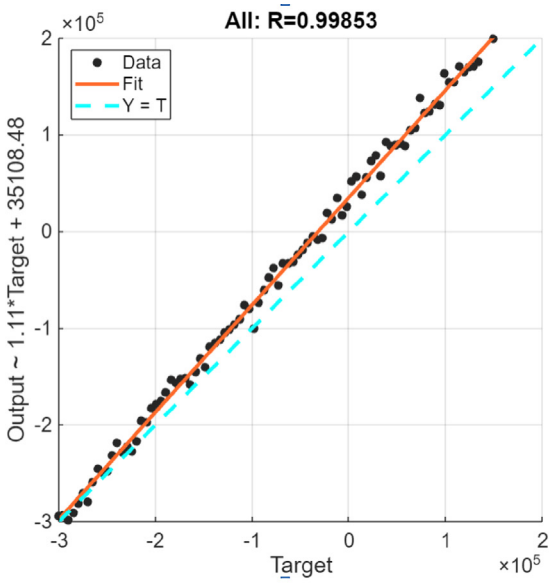

(b) Regression plot for MPC controller 2

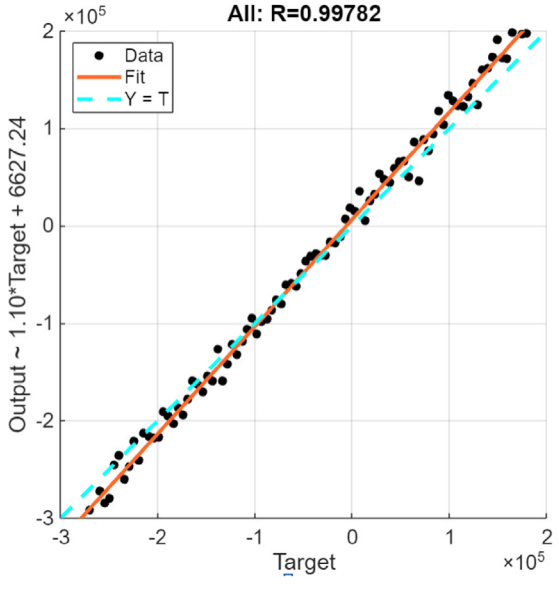

(a) Regression plot for MPC controller 3

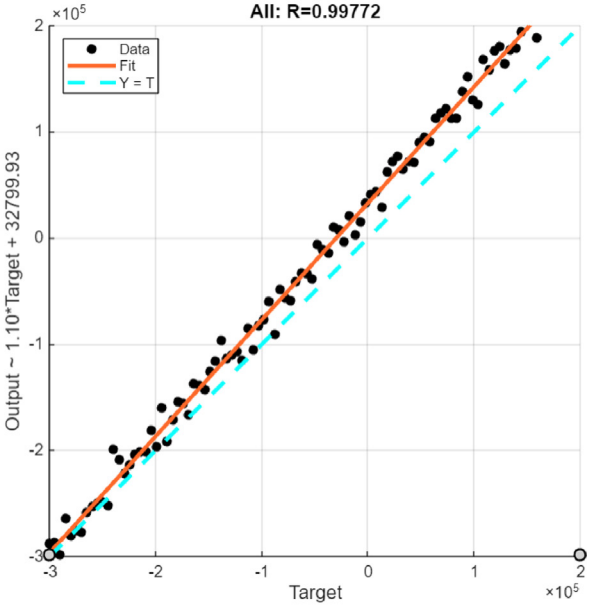

(b) Regression plot for MPC controller 4

Fig. 7. Regression plots of NN for MPC controllers.

et al., 2019). In this model, the control variable $\boldsymbol{u}(k)$ is substituted with its rate of change $\Delta\boldsymbol{u}(k)$ and the state variable $\boldsymbol{x}(k)$ is substituted with a pair of state variables $\boldsymbol{x}(k) = [\Delta\boldsymbol{x}(k)\boldsymbol{y}(k)]^T$.

$$\begin{bmatrix} \Delta\boldsymbol{x}(k+1) \\ y(k+1) \end{bmatrix} = \begin{bmatrix} \mathbf{A} & \mathbf{O}_{p\times n}{}^T \\ \mathbf{CA} & \mathbf{I}_{p\times p} \end{bmatrix} \begin{bmatrix} \Delta\boldsymbol{x}(k) \\ \boldsymbol{y}(k) \end{bmatrix} + \begin{bmatrix} \mathbf{B} \\ \mathbf{CB} \end{bmatrix} \Delta\boldsymbol{u}(k),$$
$$\boldsymbol{y}(k) = \begin{bmatrix} \boldsymbol{O}\mathbf{I}_{p\times p} \end{bmatrix} \begin{bmatrix} \Delta\boldsymbol{x}(k) \\ \boldsymbol{y}(k) \end{bmatrix}, \tag{34}$$

where $\begin{bmatrix} \mathbf{A} & \mathbf{O}_{p\times n}{}^T \\ \mathbf{CA} & \mathbf{I}_{p\times p} \end{bmatrix}$ is the augmented state matrix denoted by $\mathbf{A}_g$, $\begin{bmatrix} \mathbf{B} \\ \mathbf{CB} \end{bmatrix}$ is the augmented input matrix $\mathbf{B}_g$, and $\begin{bmatrix} O\mathbf{I}_{p\times p} \end{bmatrix}$ is the augmented output matrix $\mathbf{C}_g$. The obtained augmented model is presented as

$$\boldsymbol{y}(k) = \mathbf{C}_g\boldsymbol{x}(k). \tag{35}$$

By using the augmented model $(\mathbf{A}_g, \mathbf{B}_g, \mathbf{C}_g)$, the MPC controller predicts the output given by (Wang, 2009)

Table 1
Information about the NN process for MPC controller estimation.

Category	Information	
Dataset Acquisition	Range of Initial Angles for Simulations:	−78° to +78°
	Difference between successive initial angles:	3°
	Number of Simulations:	52
	Number of Iterations:	6000
	Number of Input Dataset Variables:	9
	Number of Output Dataset Variables:	3
	Size of dataset:	312000 × 12
Dataset Division	Training:	70 % Dataset
	Testing:	15 % Dataset
	Validation:	15 % Dataset
NN Information	NN Configuration:	Feedforward Configuration
	Training algorithm:	Levenberg Marquardt method
	Number of hidden layers:	18

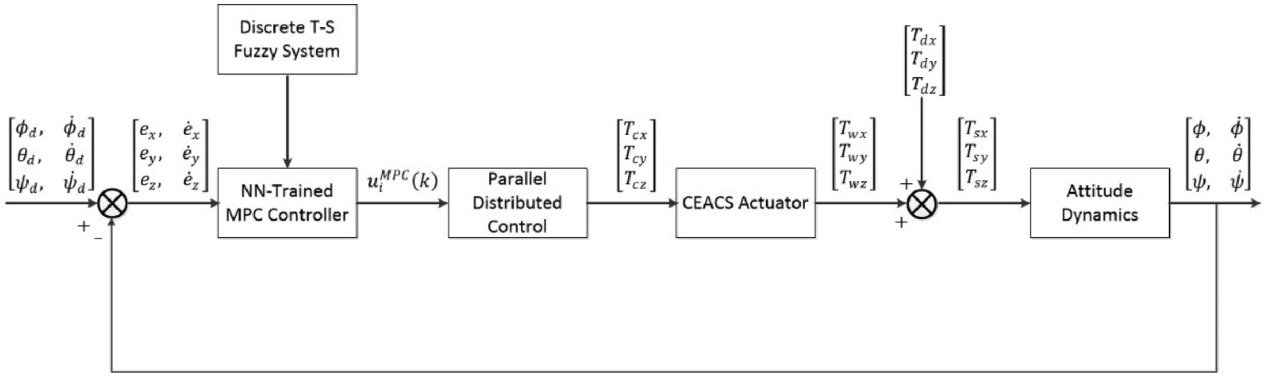

Fig. 8. D-FMPC implementation for CEACS attitude regulation.

$$\boldsymbol{y} = \mathbf{F}\boldsymbol{x}(k) + \Gamma\Delta\boldsymbol{u}, \tag{36}$$

where

$$\mathbf{F} = \begin{bmatrix} \mathbf{C}_g\mathbf{A}_g \\ \mathbf{C}_g\mathbf{A}_g^2 \\ \vdots \\ \mathbf{C}_g\mathbf{A}_g^{NP} \end{bmatrix},$$

$$\Gamma = \begin{bmatrix} \mathbf{C}_g\mathbf{B}_g & 0 & 0 & \cdots & 0 \\ \mathbf{C}_g\mathbf{A}_g\mathbf{B}_g & \mathbf{C}_g\mathbf{B}_g & 0 & \cdots & 0 \\ \vdots & \vdots & \vdots & \vdots & \vdots \\ \mathbf{C}_g\mathbf{A}_g^{N_p-1}\mathbf{B}_g & \mathbf{C}_g\mathbf{A}_g^{N_p-2}\mathbf{B}_g & \mathbf{C}_g\mathbf{A}_g^{N_p-3}\mathbf{B}_g & \cdots & \mathbf{C}_g\mathbf{A}_g^{N_p-N_c}B_g \end{bmatrix},$$

and

$$\boldsymbol{y} = \left[y(k+1|k)\ y(k+2|k)\, y(k+3|k) \cdots y\left(k+N_p|k\right)\right]^T.$$

Here, N_c denotes the number of predicted control moves needed to achieve target output, while N_p signifies the size of the prediction horizon. The primary aim of MPC is to minimize the difference between the predicted output and required output. To attain this goal, an objective function is formulated to determine an optimized control vector Δu, as presented by Wang (2009).

$$O = (\boldsymbol{r}_s r(k) - \boldsymbol{y})^T(\boldsymbol{r}_s r(k) - \boldsymbol{y}) + \Delta\boldsymbol{u}^T\,\bar{\boldsymbol{R}}\,\Delta\boldsymbol{u}, \tag{37}$$

While constraints are represented as

$$\Delta\boldsymbol{u}^{min} \le \Delta\boldsymbol{u}(k) \le \Delta\boldsymbol{u}^{max},$$
$$\boldsymbol{u}^{min} \le \boldsymbol{u}(k) \le \boldsymbol{u}^{max},$$

where $r(k)$ is the set-point, $\boldsymbol{r}_s^T = \left[\overbrace{1, 1, ..., 1}^{N_P}\right]$ is a unity vector, $\bar{\mathbf{R}} = r_w\mathbf{I}_{Nc\times Nc}$ is a cost matrix, and $r_w \ge 0$ is a user-defined variable that provides a check on the closed-loop performance. By substituting Eq. (36) in Eq. (37), and fulfilling the condition $\frac{\partial J}{\Delta U} = 0$, the optimized control vector is given by

$$\Delta\boldsymbol{u} = \left(\Gamma^T\Gamma + \bar{\mathbf{R}}\right)^{-1}\left(\Gamma^T\boldsymbol{r}_s r(k) - \Gamma^T\mathbf{F}\boldsymbol{x}(k)\right). \tag{38}$$

Table 2
Simulation scenarios for performance comparison between D-FMPC and FMPC controllers.

Scenario	Description
1	The D-FMPC controller is designed to achieve the targeted CEACS attitude-pointing accuracy, and the results are compared with those obtained using the FMPC controller.
2	The previously designed D-FMPC controller from Scenario 1 is implemented to regulate the CEACS attitude while accounting for parametric uncertainty. This uncertainty stems from the flywheel motors, simulating the impact of internal frictional torque on the flywheels. The numerical validations are then compared with those of the FMPC controller.
3	A computational comparison between the FMPC and D-FMPC controllers has been conducted in terms of both execution time and memory usage. The simulation conditions for this case are consistent with those of scenario 2.

Table 3
Simulation parameters used in CEACS attitude control system.

Parameter	Value(s)
Satellite's Mass	127.632 kg
Altitude	500 km
Orbital Period, T_o	5, 667 seconds
Flywheel's inertia	$I_w = 0.0013$ kg-m^2
Satellite's Inertia Tensor	$\begin{bmatrix} I_x \\ I_y \\ I_z \end{bmatrix} = \begin{bmatrix} 4.6 \\ 4.2 \\ 4.6 \end{bmatrix}$ kg-m^2
Flywheel's time constant	**Scenario 1** $\tau = 0.5$ s **Scenario 2–3** $\tau_1 = 1.0$ s $\tau_2 = 2.5$ s
Disturbance torques	$\begin{bmatrix} T_{dx} \\ T_{dy} \\ T_{dz} \end{bmatrix} = \begin{bmatrix} 3.34 + 7.68\cos(\omega t) \\ 3.34 + 7.68\sin(\omega t) \\ 3.34 - 7.68\cos(\omega t) \end{bmatrix} \times 10^{-5}$ Nm
Desired attitude pointing accuracy	$\lvert\phi\rvert \leq 0.1^o$ $\lvert\theta\rvert \leq 0.1^o$ $\lvert\psi\rvert \leq 0.1^o$
Actuator's constraints	$\lvert T_a\rvert \leq 0.038$ Nm
Initial Conditions	**Scenarios 1–3** $\varnothing(0) = 70^o$ $\theta(0) = 68^o$ $\psi(0) = 65^o$ $\omega_x(0) = 0^o/\text{sec}$ $\omega_y(0) = 0^o/\text{sec}$ $\omega_z(0) = 0^o/\text{sec}$ **Monte Carlo Settings (Stability Analysis)** $\begin{bmatrix} \theta_1(0) \\ \theta_2(0) \\ \theta_3(0) \\ \theta_4(0) \\ \theta_5(0) \\ \theta_6(0) \end{bmatrix} = \begin{bmatrix} 78^o \\ 50^o \\ 30^o \\ -78^o \\ -50^o \\ -30^o \end{bmatrix}$
MPC Settings:	
Prediction horizon	$N_p = 20$
Control horizon	$N_c = 10$
Sampling time	$T_s = 2$ sec
Tuning parameter	$r_w = 100$
Number of hidden layers	$N = 18$
Angular velocities limits	$-0.00174 \leq \omega_x \leq 0.00174$ rad/sec $-0.00174 \leq \omega_y \leq 0.00174$ rad/sec

At last, the control vector $\boldsymbol{u}(k)$ produced by the MPC controller is calculated as

$$\boldsymbol{u}(k) = \boldsymbol{u}(k-1) + \Delta\boldsymbol{u}(\boldsymbol{k}). \tag{39}$$

4.2. Deep layer neural network

A NN is an information processing model, that closely follows the biological nervous system such as the brain process information. The basic processing element of NN is the neuron, which works in a group with other Neurons in the form of a network to solve specific problems. A network is the interconnection of these processing units, whereas each unit has its I/O features and performs local computing. The numerical output of any neuron mainly depends on the I/O characteristics, interconnection to other units and external inputs. In literature, various NN-based configurations have been available however, the feedforward NN model is mostly used in industrial applications as shown in Fig. 5 (Biggs and Fournier, 2019). In this approach, the input layer of neurons is linked to the output layer of neurons through one or more intermediate layers, and these intermediate layers are famously known as hidden layer(s). The multilayer NN is generally known by various names such as deep-layer NN, and multi-layer perceptions. However, this multi-layer NN is classified as a deep learning technique as shown in Fig. 6 (Biggs and Fournier, 2019). The output of a layer is given by

$$\alpha^1 = \sigma^1\left(W^1\rho + b^1\right) \tag{40}$$

$$\alpha^{m+1} = \sigma^{m+1}(W^{m+1}\alpha^m + b^{m+1}) \quad \text{for } m = 2, .., M-1 \tag{41}$$

where $\rho \in \mathbb{R}^{S^0\times 1}$ is the input, α^m is the output of layer m, $W^m \in \mathbb{R}^{S^m\times S^{m-1}}$ and $b^m \in \mathbb{R}^{S^m\times 1}$ are the weights and biases of layer m, σ^m is the activation function of layer m, and S^m represents the number of neurons in the layer m.

Here, identity function is used by the output layer, while the hidden layer uses log-sigmoid function as the activation function

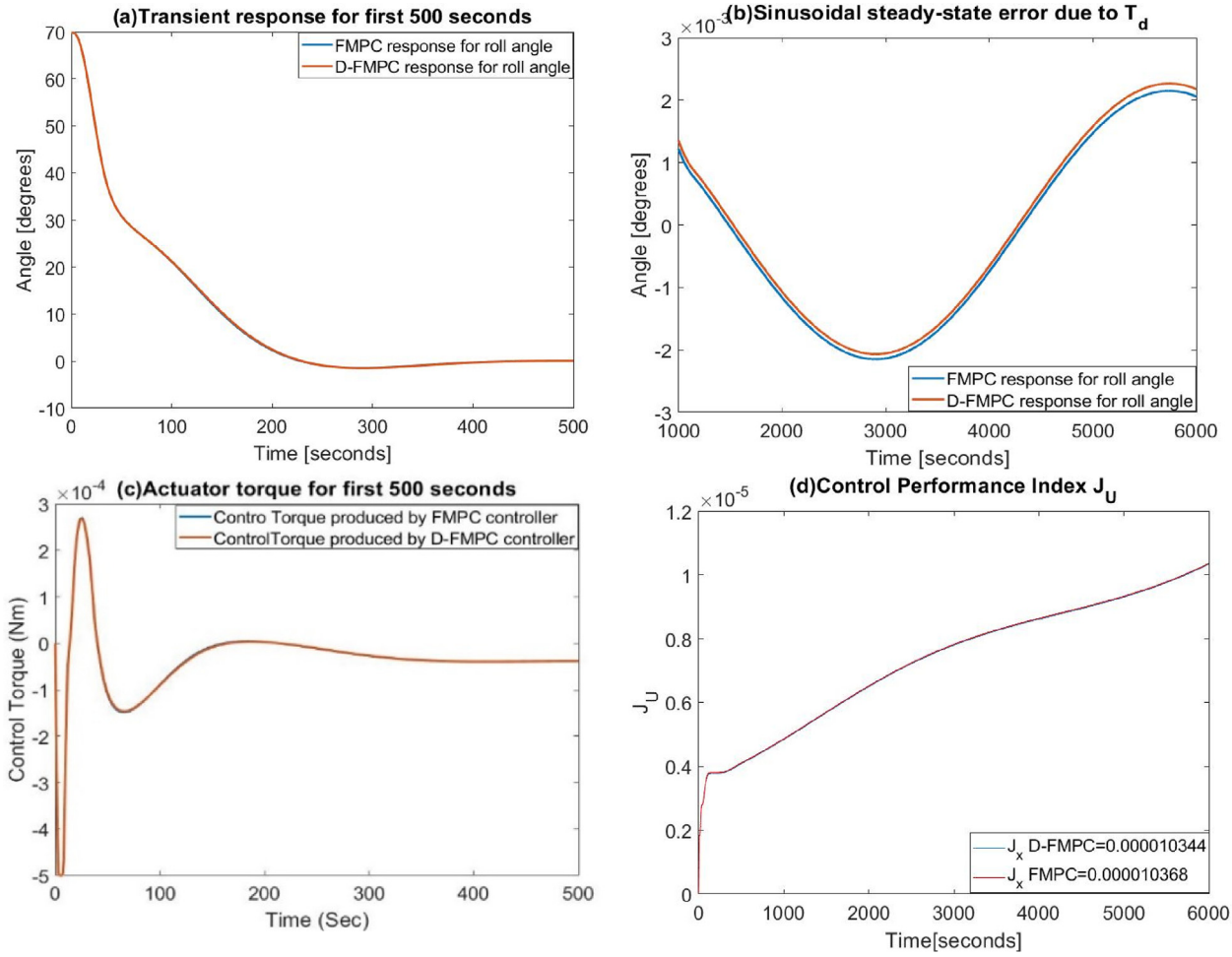

Fig. 9. Scenario 1: FMPC and D-FMPC roll angle results.

$$\sigma(n) = \frac{1}{1+e^{-n}} \tag{42}$$

where e is the Euler's number. The output of the sigmoid function lies between 0 and 1. As the input n becomes very large, the output approaches 1, and as n becomes very low, the output approaches 0.

Training a NN is done by providing a data set of target input–output pair and tuning the weights and biases to ensure the predicted output of the NN closely resembles the targeted output for the same inputs. The core objective is not interpolation, but to generalize the trained NN model for any new input that exists between the range of training sets. For a given input–output data set $(\rho^q, t^q)_{q=1,2,..,Q}$ for Q training dataset, the following objective function is used by the NN for training purpose (Biggs and Fournier, 2019)

$$Obj^{tr}(\boldsymbol{\delta}) = \frac{1}{Q}\sum_{q=1}^{Q}(t^q - \alpha^q(\boldsymbol{\delta}))^T(t^q - \alpha^q(\boldsymbol{\delta})) \tag{43}$$

Here, $\boldsymbol{\delta} \in \mathbb{R}^{\sum_{m=0}^{M-1}(S^m+1)S^{m+1}}$ represents a vector that includes all biases and weights of the NN. The above cost function can be simplified as

$$Obj^{tr}(\boldsymbol{\delta}) = \boldsymbol{\eta}(\boldsymbol{\delta})^T\boldsymbol{\eta}(\boldsymbol{\delta}) \tag{44}$$

where $\boldsymbol{\eta}$ is the vector containing Q error vectors. The objective function is minimized by using the Levenberg Marquardt algorithm and the updated $\boldsymbol{\delta}$ at every iteration is given by

$$\boldsymbol{\delta}_{k+1} = \boldsymbol{\delta}_k - \left[J^T(\boldsymbol{\delta}_k)J(\boldsymbol{\delta}_k) + c_k\right]^{-1}J^T(\boldsymbol{\delta}_k)\boldsymbol{\eta}(\boldsymbol{\delta}_k) \tag{45}$$

where, c_k is directly related with the minimization of the objective function, as the updated weight reduces the objective function Obj, c_k also gets reduced and vice-versa. A continuous decrease in c_k converges the predicted output to the target output. Here, J is the cost Jacobian matrix represented by

$$J = \frac{\partial \boldsymbol{\eta}}{\partial \boldsymbol{\delta}} \in \mathbb{R}^{(s^mQ)\times\left(\sum_{m=0}^{M-1}(s^m+1)s^{m+1}\right)} \tag{46}$$

Here, J is obtained by the back propagation algorithm as derived in (Battipede, et al., 2003).

4.2.1. Training of neural network

In this work, the dataset necessary for training, testing, and validating the neural network model is acquired through simulations of the FMPC for satellite CEACS atti-

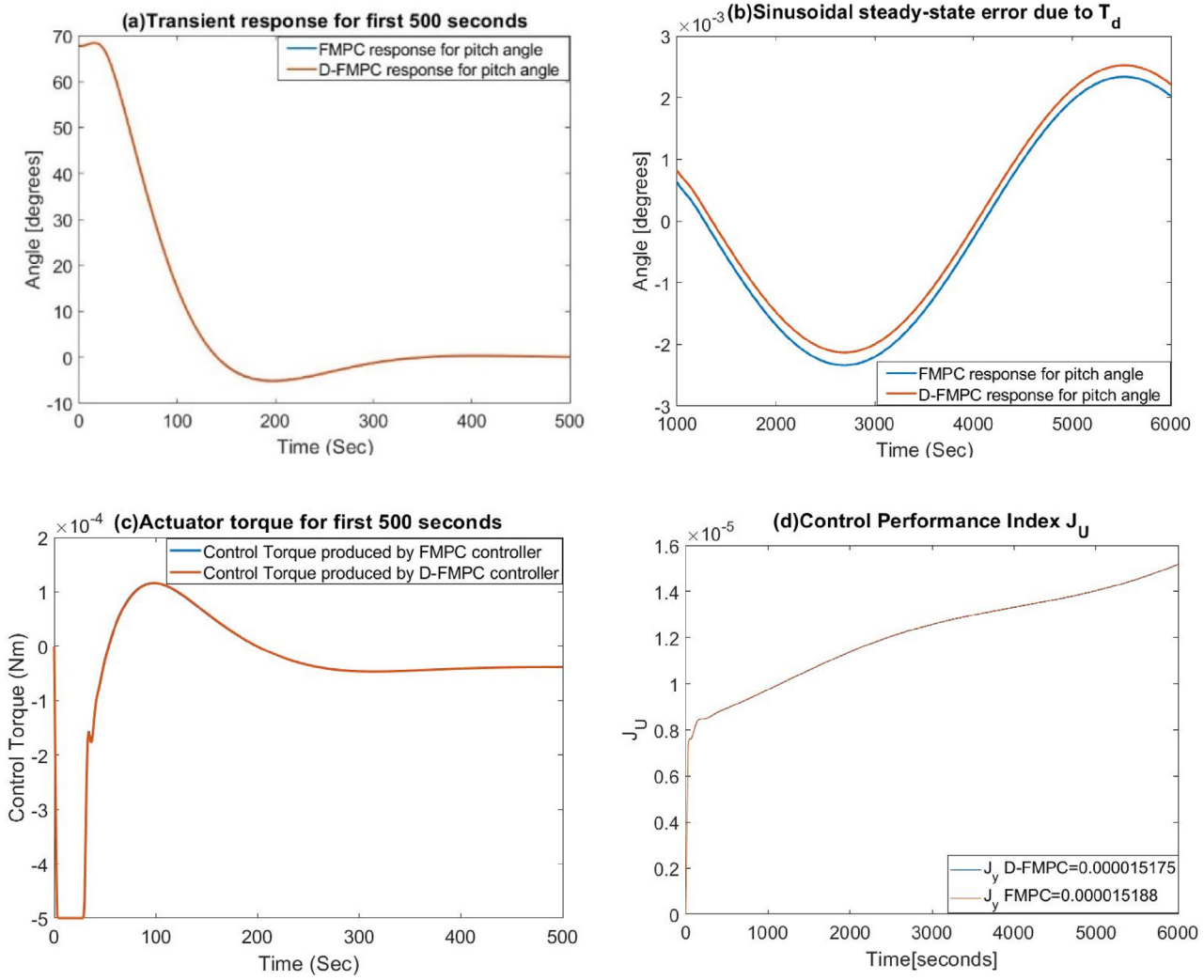

Fig. 10. Scenario1: FMPC and D-FMPC pitch angle results.

tude control. Simulated data is employed due to the absence of real-time data for FMPC-based CEACS attitude control. Nevertheless, the methodology for training the neural network mirrors that employed for real-time data, as documented in previous studies (Biggs and Fournier, 2019; Sivaprakash and Shanmugam, 2005; Kim et al., 2016).

The input–output dataset encompasses the error $\{e_x, e_y, e_z\}$, change in error $\{\dot{e}_x, \dot{e}_y, \dot{e}_z\}$, and current output values $\{\phi, \theta, \psi\}$ of the satellite attitude as input, with the control torques $\{T_{cx}, T_{cy}, T_{cz}\}$ produced by the MPC controller serving as the target output. The quality of the training process is directly related to the quality and size of the dataset. To ensure robust training, simulations of the FMPC controller have been conducted for a large number of initial conditions, spanning a range from $-78°$ to $+78°$. These simulations account for external disturbance torques, actuator constraints, and CEACS parametric uncertainty. Furthermore, to effectively approximate the performance of the FMPC controller, the difference between initial conditions for two simulations is set to 3°, resulting in a total of 52 simulations.

In each simulation, 6000 iterations were conducted, resulting in the acquisition of an input–output dataset containing 312,000 values. This complete dataset is partitioned into three segments: 70 % for training, 15 % for testing, and 15 % for validation purposes. Furthermore, the NN employs eighteen hidden layers, selected through tuning, to successfully replicate the computationally intensive FMPC controller. The regression plots of the trained NN are depicted in Fig. 7. A NN with a substantial number of hidden layers is commonly referred to as deep learning or a deep NN.

From Fig. 7, it is evident that the deep-layer NN has been effectively trained using the simulated data derived from the implemented FMPC controller for the attitude regulation of CEACS. It is seen in the regression plot for each MPC controller, the fitted model overlaps the ideal perfect fit represented by the dash line. Thus, it shows that model provides an excellent fit to the data, with the pre-

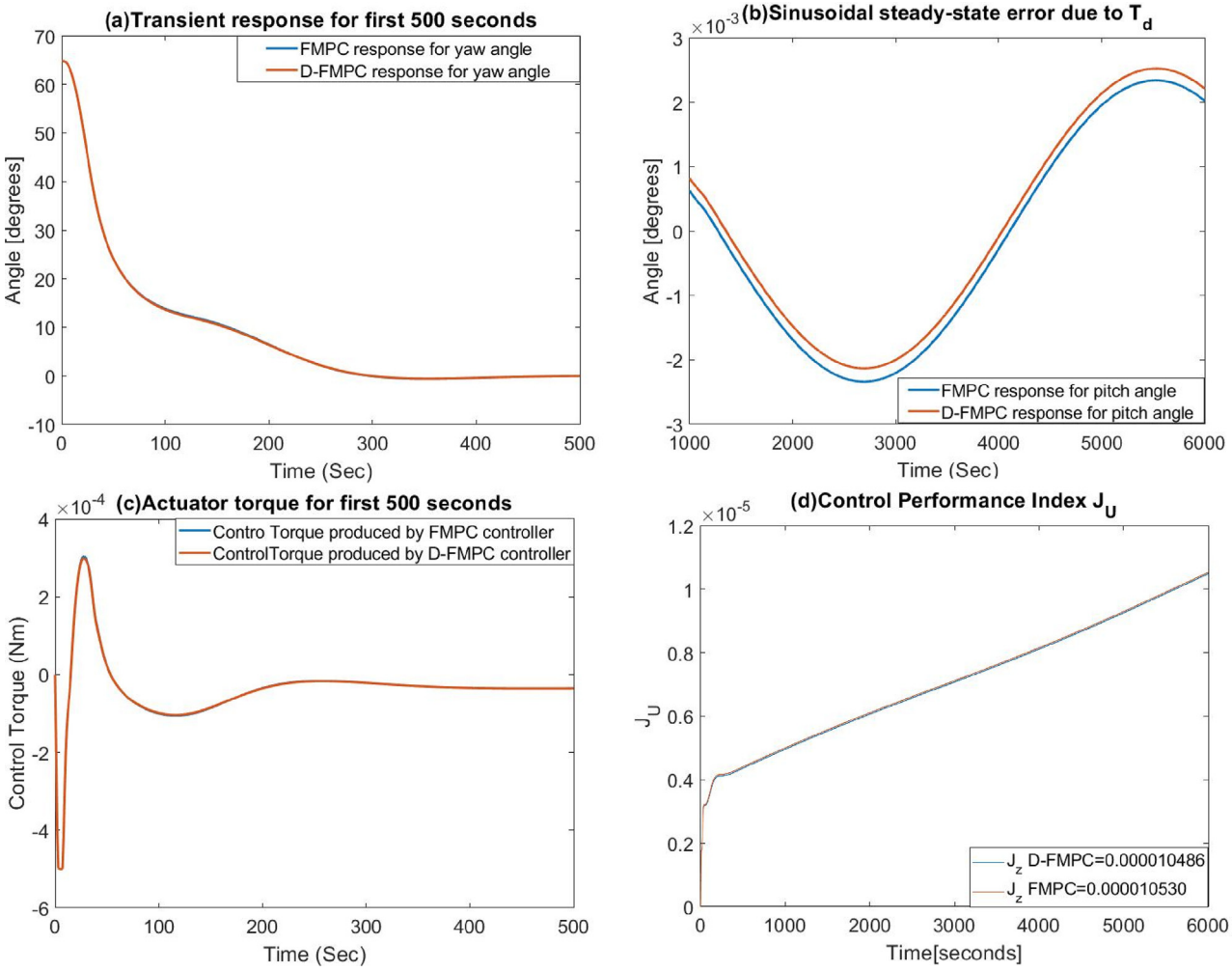

Fig. 11. Scenario 1: FMPC and D-FMPC yaw angle results.

dicted outputs nearly perfectly matching the actual target values. The correlation coefficient (**R**) almost approaches unity for each regression plot. The high correlation coefficient and the close alignment of the model fit line with the ideal fit line both indicate that the regression model is highly effective in capturing the relationship between the inputs and outputs. These findings can be explicitly validated by witnessing a very few predicted values deviating from the target values as shown in Fig. 7 as well. Thus, it is assured that trained NN based controllers can replicate the MPC controllers.

The brief overview of information about the training of NN models for the approximation of MPC controllers has been presented in Table 1.

4.3. D-FMPC controller implementation

The D-FMPC controller is implemented by replacing the computationally intensive MPC controller with its trained deep-layer NN model as shown in Fig. 8.

5. Numerical results

The effectiveness of the D-FMPC controller is investigated by performing the numerical treatments, which have been presented in this section. For validation purposes, the numerical results are compared with the FMPC controller in terms of pointing accuracies, oscillatory response, percentage overshoot, and actuator constraints violations. The CEACS attitude control results have been analyzed in three scenarios. In first scenario, the numerical results of the D-FMPC controller are compared with the computationally intensive FMPC controller for the satellite CEACS attitude regulation with larger initial angles, i.e., $\pm 70°$. The initial angles are chosen largely to cover the entire earth in triangulation at about 500 km altitude. In the second scenario, the robustness of the D-FMPC controller is investigated against the CEACS parametric uncertainty. The CEACS parametric uncertainty includes the variation in frictional torque of the counter-rotating flywheels. The frictional torque is experienced by the flywheel due to friction

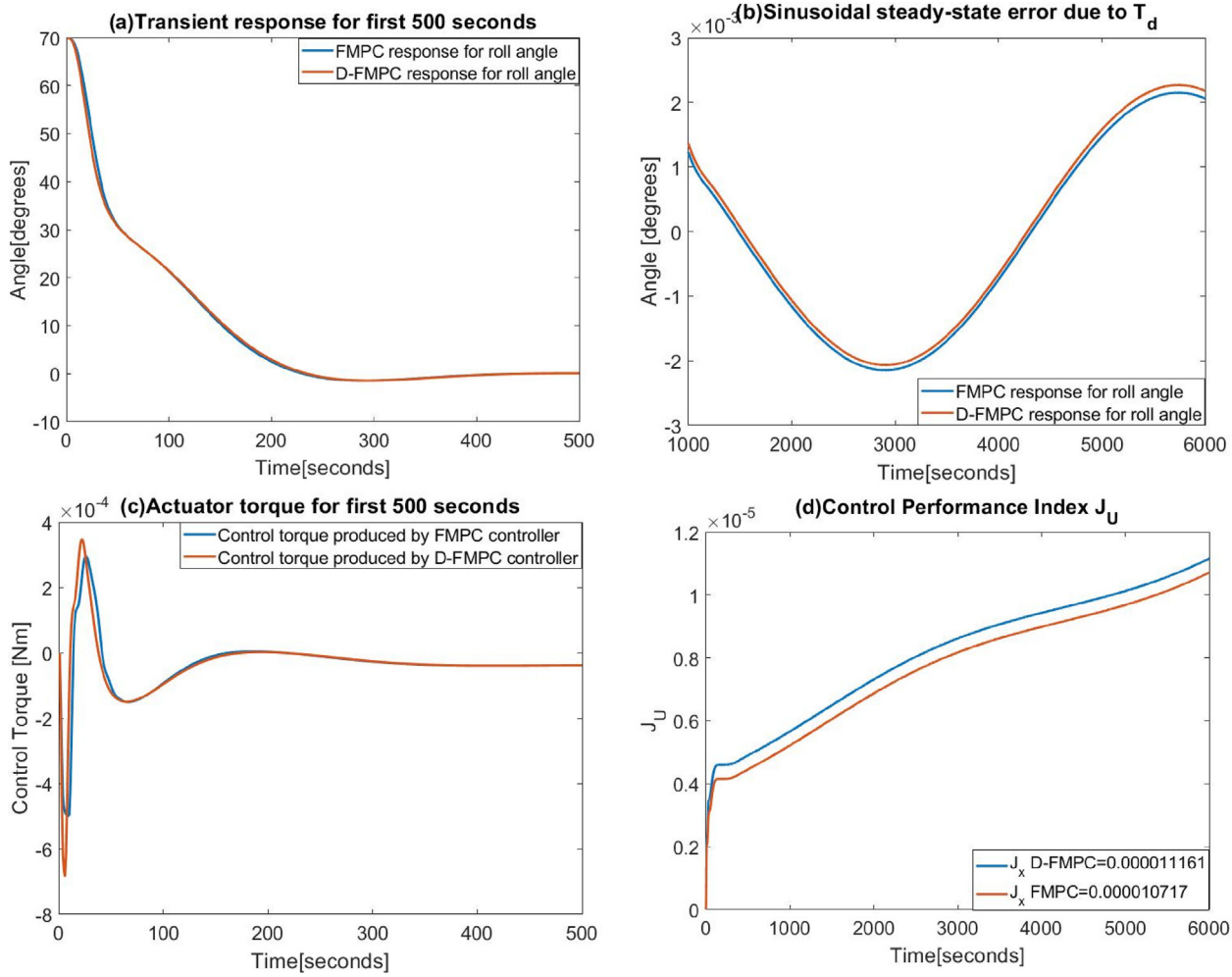

Fig. 12. Scenario 2: FMPC and D-FMPC roll angle results.

between its moving parts, i.e., bearings and other mechanical parts. Two flywheels may have the same frictional torques due to a number of reasons such as same materials used, the design of the flywheel, the lubrication of its components, and the speed at which it rotates. However, frictional torque may vary over time due to wear and tear of mechanical components and change in operating conditions, i.e., variation in the speeds of counter-rotating flywheels. Thus, the frictional torque variations contribute to variation in the time constants of the counter-rotating flywheels in the CEACS system. Similarly, the variation in flywheel's inertia of counter-rotating flywheels may also contribute to change in time constants and consequently, it adds a biased torque to the net torque produced by the CEACS (Aslam et al., 2022). The results governed by the proposed controller are compared with the FMPC controller to validate the true replication of the FMPC controller. In the third scenario, a computational comparison between the FMPC and D-FMPC controllers is presented to validate the computational efficiency-based superiority of the D-FMPC controller over the FMPC controller. This comparison is expressed in terms of the execution time and memory usage of the code, as discussed by Kim et al. (2016).

The environmental disturbance torques used here is the joint contribution of all environmental disturbance torques. However, the gravitational and aerodynamic torques are almost equal at altitude $\leq$450 km (Liop et al., 2019). Here, the gravitational torque is included as a sinusoidal wave in the disturbance torques. This disturbance torque exhibit magnitudes typically ranging from 10^{-4} to 10^{-6} Nm LEO, as reported in (Zagorski, 2012). It is noteworthy that satellites with reduced inertia tend to encounter smaller disturbance torques.

A brief summary of the presented scenarios is given in Table 2.

The details about the simulation settings and satellite reference mission are given in Table 3. The numerical results of all scenarios are shown in Figs. 9–16.

Scenario 1 provides the numerical results of the F-MPC and D-FMPC controllers for the CEACS attitude regula-

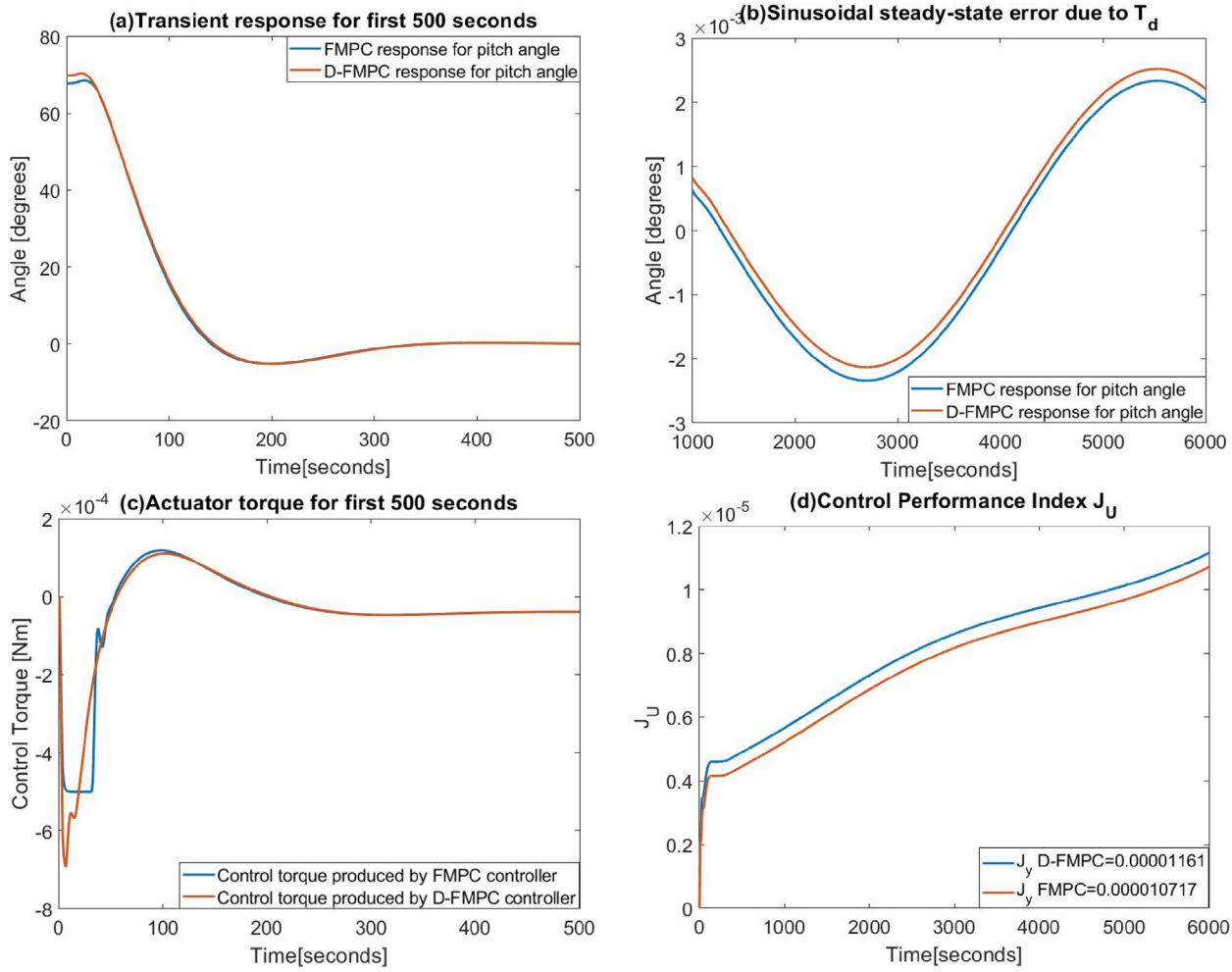

Fig. 13. Scenario 2: FMPC and D-FMPC pitch angle results.

tion in the presence of actuator constraints and external disturbance torques.

From part (a) of Figs. 9–11, it can be seen that both FMPC and D-FMPC controllers produce a smooth transient response of attitude angles. Both controllers effectively regulate the CEACS attitude with a minimum steady-state error in the presence of external disturbance torques. However, the FMPC controller slightly produces a better pointing accuracy than its replica D-FMPC controller as shown in Figs. 9(b)–11(b). Both controllers keep the control torques within the actuator's operational limits as shown in Figs. 9(c)–11(c). However, it is also observed in Figs. 9–11 that the initial negative value of the control torques occur as the satellite initiates its motion from a state of rest, starting with positive initial angles. This phenomenon is analogous to the restorative torque effect observed in mass-spring-damper systems. In order to evaluate a controller in terms of energy consumption, integral of the squared control torque is used as a quantitative metric represented by J_U (performance index) (Aslam et al., 2022). The parameter J_U reflects the amount of torque required to produce the desired pointing accuracy. This performance index directly relates to the onboard power consumed by the CEACS, as producing the required torque requires speeding up one flywheel and slowing down the counter flywheel. The speeding up of a flywheel consumes more electrical power and similarly slowing down the speed of flywheel decreases the amount of energy stored in it. Thus, a larger J_U correlates with a higher power consumption by the CEACS system. This can be further verified in Varatharajoo (2006b). According to Figs. 9(d)–11(d), the values of J_U for D-FMPC controller are slightly smaller than the performance index values of FMPC controller. Thus, D-FMPC controller consumes comparatively less onboard power than its counterpart. However, it is also seen that the accumulating control torque is required to maintain the desired pointing accuracies.

The overall results demonstrate that the proposed computationally efficient Deep Learning-based D-FMPC controller can achieve the desired CEACS attitude-pointing accuracy while staying within the actuator limits for control torques, similar to the performance of the FMPC controller.

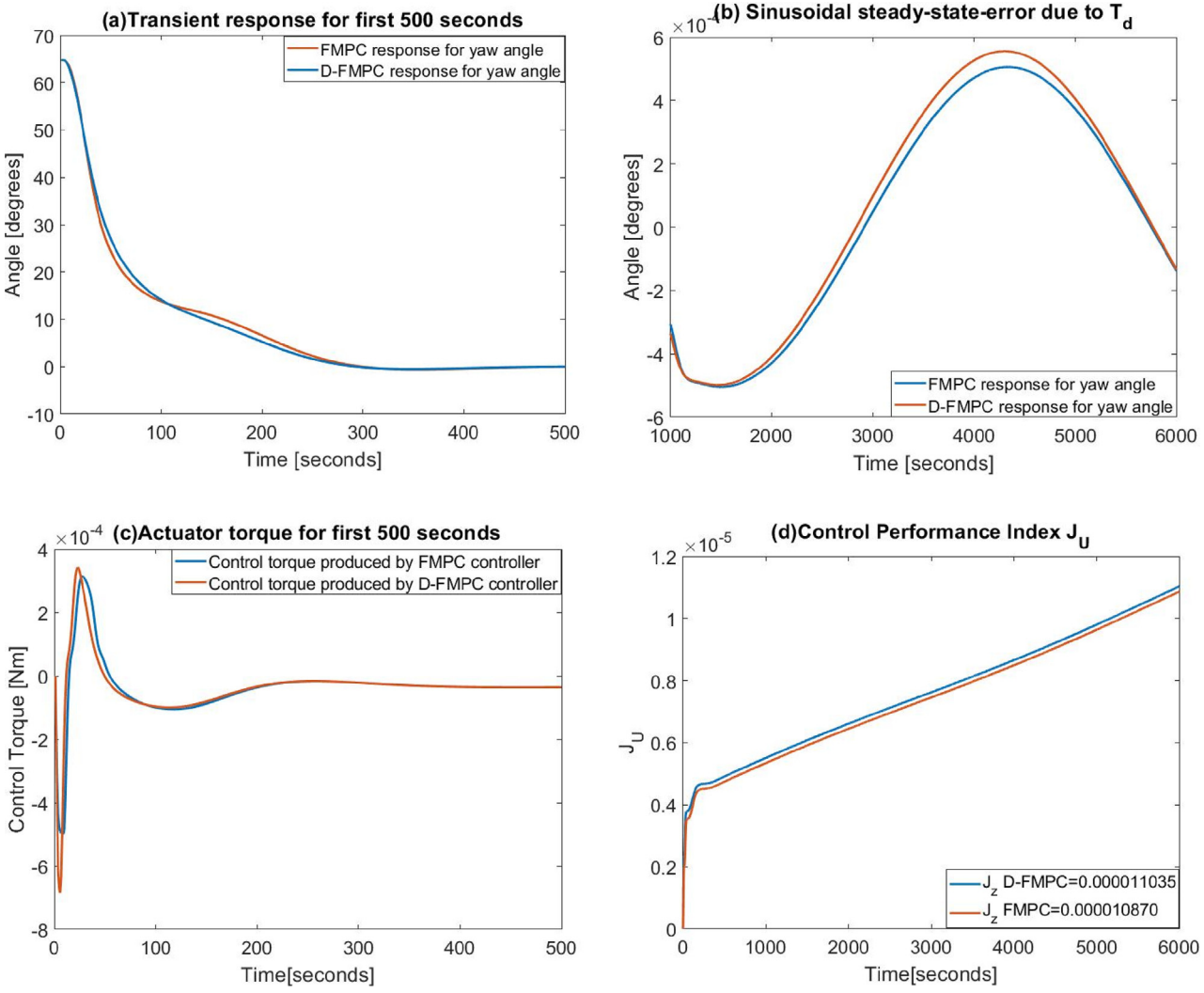

Fig. 14. Scenario 2: FMPC and D-FMPC yaw angle results.

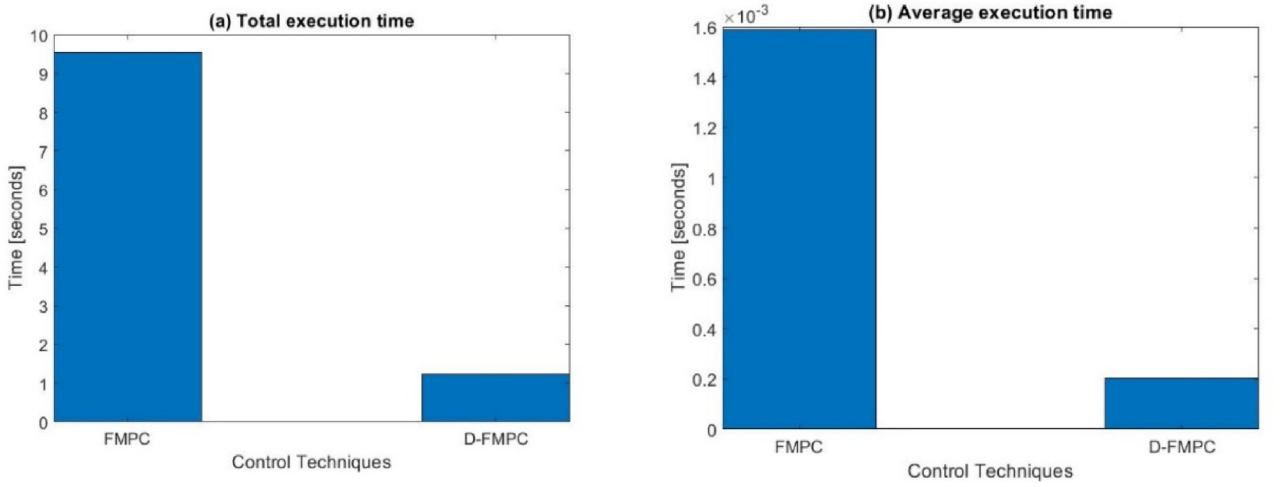

Fig. 15. Scenario 3: Computational comparison between the FMPC and D-FMPC controllers in terms of execution time.

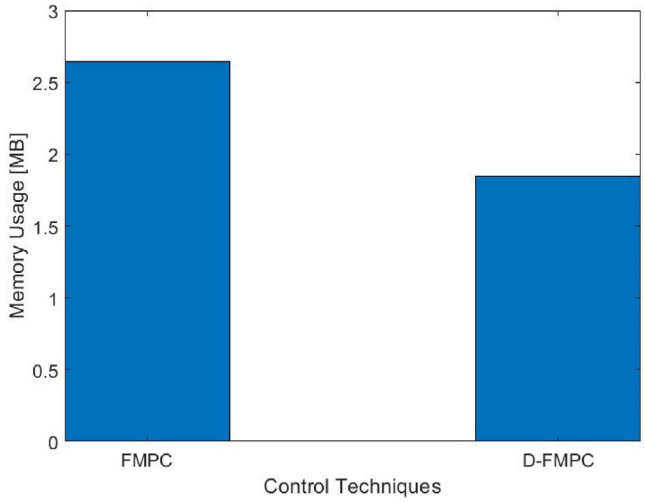

Fig. 16. Scenario 3: Computational comparison between the FMPC and D-FMPC controllers in terms of memory usage.

Scenario 2 provides the numerical validations of the both controllers FMPC and D-FMPC in the presence of parametric uncertainty.

From part (a) of Figs. 12–14, it can be observed that both the controllers produce a smooth and slow transient response of all attitude angles and successfully converge them to the desired CEACS pointing accuracy as shown in part (b) of Figs. 12–14. However, the transient response governed by the D-FMPC slightly deviates from its comparative controller. It is also observed that the FMPC offers slightly better pointing accuracy as compared to its replica D-FMPC controller. Although, both controllers ensure that the control torques remain within the torque producing capabilities of the actuators to prevent actuator saturation problem. But due to the flywheels frictional differences, slight oscillations have been produced by the CEACS actuation at the start as shown in Figs. 12(c)–14(c). However, as time progresses, both the controllers successfully counter the effect of biased torque governed by the time constant difference in both flywheels by producing the optimized control torques. Figs. 12(d)–14(d) show that the presence of parametric uncertainty contributes to the slight increase in the cost value of the D-FMPC controller.

Thus, it can be concluded that the proposed D-FMPC controller performs almost similarly to the FMPC controller in both scenarios and shows robustness against the parametric uncertainty. The performance results in terms of attitude pointing accuracies, oscillatory transient, and percentage overshoot are tabulated in Table 4.

Scenario 3 validates the outcome of approximating the computationally intensive FMPC controller by a computationally efficient D-FMPC controller.

A computational comparison between the two controllers is conducted, considering execution time and memory usage. The simulations are performed in MATLAB R2018a, and the computer hardware specifications consist of an Intel Core i7-1165G7 11th Generation quad-core processor running at 2.8 GHz, 8 GB RAM, and a 256 GB SSD Hard disk. The operating system is Microsoft Windows 10 Pro.

From Fig. 15(a), it is seen that the total execution time of the FMPC controller is 9.54 s, and that of the D-FMPC controller is only 1.226 s. The total execution time includes 6000 iterations of the code. Similarly, the FMPC controller takes on average 1.59 ms to complete one iteration and on the other hand D-FMPC only takes 0.205 ms on average to complete a single iteration as shown in Fig. 15(b). The memory usage plot given in Fig. 16 shows that the FMPC controller used 2.642 MB of memory for storing the information in variables while, the D-FMPC controller used 1.846 MB of memory to store its variables. Thus, it validates that the D-FMPC controller offers a smaller computational burden to the satellite compared to the FMPC controller, while performing the CEACS attitude regulation task equally well as its counterpart.

6. Stability demonstration

Stability analysis is a crucial aspect as it ensures the closed-loop system operates predictably and reliably. In conventional control systems, stability theorems are used to investigate the stability of closed-loop systems. These theorems are based on mathematical principles and models that govern the system's operation. However, a deep-layer NN-based controller contains thousands of nodes and layers, making it impractical to prove the stability of each node in the path using explicit mathematical equations. Analyzing the stability of an NN-based controller becomes more challenging when it fully replaces other controllers. A feasible solution to this problem is a two-step process. The first step involves rigorous training of the NN using a large,

Table 4
Numerical results of CEACS.

Scenario	Controller	Pointing Accuracy			Oscillatory Transient (Yes/No)			Percentage Overshoot (%)		
		Roll	Pitch	Yaw	Roll	Pitch	Yaw	Roll	Pitch	Yaw
1	FMPC	0.0021°	0.0023°	0.00050°		No		2.11	7.57	0.88
	D-FMPC	0.0022°	0.0025°	0.00055°		No		2.11	7.57	0.88
2	FMPC	0.0021°	0.0023°	0.00050°		No		2.11	7.57	0.88
	D-FMPC	0.0022°	0.0025°	0.00055°		No		2.11	7.57	0.88

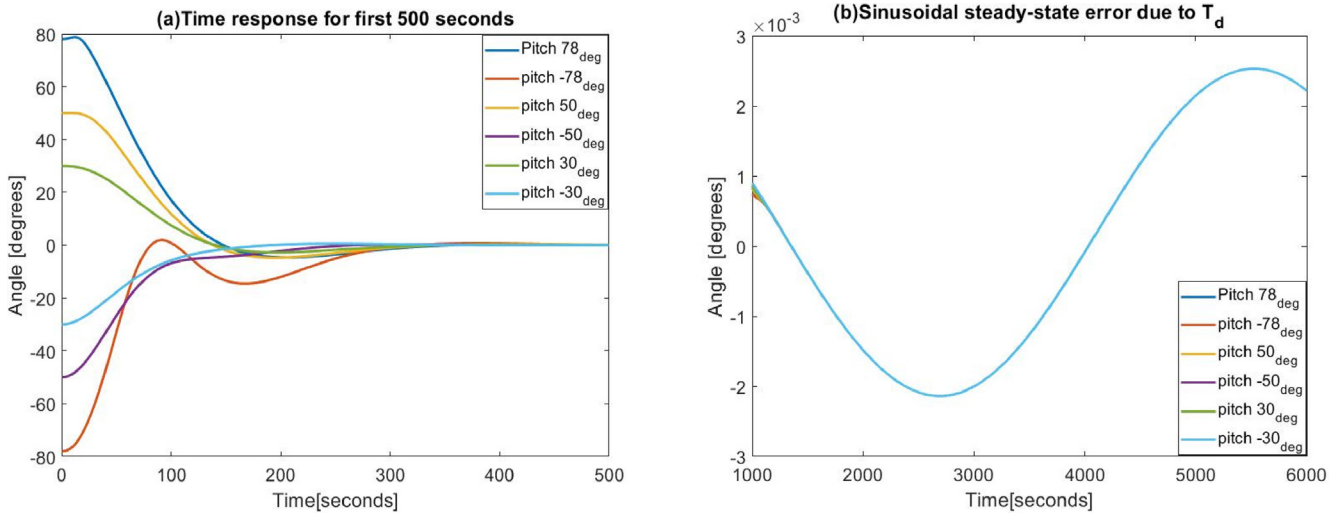

Fig. 17. Pitch angle regulation with Monte Carlo scenario in presence of uncertainty.

refined dataset, and the second step involves investigating its performance under a high and wide range of initial conditions. Therefore, to demonstrate the stability of the D-FMPC controller a Monte Carlo simulation environment has been implemented. Here, a wide range of both positive and negative initial angles have been used. However, for demonstration purposes, only pitch angle regulation has been presented for six higher initial angles as an example. The initial angles have been given in Table 2. The numerical results have been shown in Fig. 17.

From Fig. 17(a), it is seen that the CEACS attitude regulation with all the positive and negative initial angles successfully converge within 400 s and at the steady-state, all the pitch angle trajectories obtain the same pointing accuracy of 0.0025^{o} as shown in Fig. 17(b). Thus, it shows that the D-FMPC controller can successfully regulate the CEACS attitude pointing for the entire range of $\pm 78°$.

7. Conclusions

This novel work contributes to the design of a computationally efficient D-FMPC attitude controller, whereby a deep learning-based replicates a computationally complex FMPC controller to regulate the CEACS attitude pointing. For the performance investigation of the proposed controller, numerical results have been presented in three scenarios. Scenario 1 demonstrates the performance of the D-FMPC controller in comparison to the FMPC controller for the CEACS attitude pointing in the presence of external disturbance torques and actuator constraints. Scenario 2 investigates the robustness of both controllers against parametric uncertainty; here, the frictional torque difference between the counter-rotating flywheels is considered. Scenario 3 validates that the D-FMPC controller is more computationally efficient than the FMPC controller, enhancing its feasibility for regulating the satellite CEACS attitude. The stability of the D-FMPC controller has been demonstrated through the Monte Carlo simulation environment and the proposed controller successfully regulates the CEACS attitude pointing within $\pm 78°$. The numerical results have shown that the D-FMPC controller performs equally well as the FMPC controller, by achieving the desired pointing accuracy and maintaining the actuator torques within the prescribed actuator constraints. Moreover, the proposed controller D-FMPC shows robustness against frictional torque variations. Thus, it validates the computationally efficient D-FMPC controller can easily replace the computationally intensive FMPC controller, and it can be considered a potential CEACS attitude controller for smaller satellites.

The design approach of D-FMPC controller provides an opportunity to replicate any computationally intensive controller with a deep learning based computationally efficient controller suitable for any smaller satellite with a limited computational capability. The results can be considered as an example to design an independent deep learning-based attitude controller in contrast to only using this approach for estimation of unknown parameters to integrate robustness in the base line controller. In addition, the proposed deep-learning solution can serve as a potential precursor to other novel deep-learning based satellite attitude controllers.

It is important to acknowledge certain limitations when training the neural network with simulated data to approximate a sophisticated control technique. Specifically, the effectiveness of the D-FMPC controller may be constrained within a specific altitude range and it may have limited tolerance for white noise in real-time scenarios. Consequently, the implementation of the D-FMPC controller in real-world scenarios may necessitate the incorporation of additional features such as self-learning algorithms or corrective capabilities.

Future CEACS studies on the adaptive deep learning-based attitude control techniques to handle the unknown

external disturbance torques in addition to the CEACS parametric uncertainties, and actuator constraints is highly desirable.

CRediT authorship contribution statement

Sohaib Aslam: Writing – original draft, Software, Methodology, Investigation, Conceptualization. **Yew-Chung Chak:** Writing – review & editing, Validation, Supervision, Methodology, Formal analysis. **Mujtaba Hussain Jaffery:** Writing – review & editing, Supervision, Resources, Project administration, Formal analysis. **Renuganth Varatharajoo:** Writing – review & editing, Validation, Supervision, Resources, Project administration, Formal analysis, Conceptualization. **Yury Razoumny:** Writing – review & editing, Supervision, Formal analysis.

Declaration of competing interest

The authors declare that they have no known competing financial interests or personal relationships that could have appeared to influence the work reported in this paper.

Acknowledgements

This paper has been supported by the Deakin University, Australia, COMSATS University Islamabad (Lahore Campus), Pakistan, the Universiti Putra Malaysia (UPM) Research University Grant, Malaysia, and the Peoples' Friendship University of Russia (RUDN), University Strategic Academic Leadership Program, Russia.

References

Ashraf, M.S., Sajjad, M.U., Haider, F., et al., 2020. Model predictive control implementation for mimo system in presence of soft constraints and nonlinear disturbance. In: Proceedings of International Conference on Electrical, Communication and Computer Engineering, Istanbul, Turkey. https://doi.org/10.1109/ICECCE49384.2020.9179446.

Aslam, S., Chak, Y.C., Jaffery, M.H., Varatharajoo, R., 2022. The fuzzy PD control for combined energy and attitude control system. Aircr. Eng. Aerosp. Technol. 94 (10), 1806–1824. https://doi.org/10.1108/AEAT-05-2021-0144.

Aslam, S., Chak, Y.C., Jaffery, M.H., Varatharajoo, R., Ansari, E.A., 2023. Model predictive control for Takagi-Sugeno fuzzy model-based Spacecraft combined energy and attitude control system. Adv. Space Res. 71 (10), 4155–4172. https://doi.org/10.1016/j.asr.2022.12.045.

Ban, Y.S., Varatharajoo, R., Ovchinnikov, O., 2012. H_2 optimal control solution for a combined energy and attitude control system. Acta Astronaut. 76, 79–83. https://doi.org/10.1016/j.actaastro.2012.02.013.

Ban, Y.S., Varatharajoo, R., 2013. H_∞ control option for a combined energy and attitude control system. Adv. Space Res. 52 (7), 1378–1383. https://doi.org/10.1016/j.asr.2013.07.006.

Battipede, M., Gili, P., Massotti, L., 2003. Neural and LQR optimal attitude control of a flexible micro-satellite. In: AIAA Guidance, Navigation, and Control Conference and Exhibit. AIAA. https://doi.org/10.2514/6.2003-5434.

Biggs, J.D., Fournier, H., 2019. Neural-network-based optimal attitude control using four impulsive thrusters. J. Guid. Control Dyn. 43 (3), 1–11. https://doi.org/10.2514/1.G004226.

Chak, Y.-C., Varatharajoo, R., 2014. A heuristic cascading fuzzy logic approach to reactive navigation for UAV. ILUM Eng. J. 15, 69–85. https://doi.org/10.31436/iiumej.v15i2.482.

Chak, Y.-C., Varatharajoo, R., 2015. A novel design of spacecraft combined attitude and sun tracking system using versatile fuzzy controller. Aircr. Eng. Aerosp. Technol. 87 (6), 530–539. https://doi.org/10.1108/AEAT-06-2014-0099.

Chak, Y.-C., Varatharajoo, R., 2017. Fuzzy switch-gain sliding mode control for spacecraft combined attitude and sun tracking system. Adv. Astronaut. Sci. 161, 13–32.

Chak, Y.-C., Varatharajoo, R., 2018. A parallel distributed compensation approach to fuzzy control of spacecraft combined attitude and sun tracking. Int. J. Eng. Technol. 7, 28–32. https://doi.org/10.14419/ijet.v7i4.13.21324.

Chak, Y.-C., Varatharajoo, R., Assadin, N., 2021. Adaptive fuzzy Jacobian control of spacecraft combined attitude and Sun tracking system. Aircr. Eng. Aerosp. Technol. 93, 1–14. https://doi.org/10.1108/AEAT-02-2020-0038.

Eshghi, S., Varatharajoo, R., 2014. Sliding mode control techniques for combined energy and attitude control system. Appl. Mech. Mater. 629, 310–317. https://doi.org/10.4028/www.scientific.net/AMM.629.310.

Eshghi, S., Varatharajoo, R., 2017. Singularity-free integral-augmented sliding mode control for combined energy and attitude control system. Adv. Space Res. 59 (2), 631–644. https://doi.org/10.1016/j.asr.2016.10.007.

Flatley, T., 1985. Tetrahedron array of reaction wheels for attitude control and energy storage. 20th Proceedings of Intersociety Energy Conversion Engineering Conference, Warrandale.

George, A.D., Wilson, C.M., 2018. Onboard processing with hybrid and reconfigurable computing on small satellites. Proc. IEEE 106 (3), 458–470. https://doi.org/10.1109/JPROC.2018.2802438.

Giron-Sierra, J.M., Ortega, G.A., 2002. A survey of stability of fuzzy logic control with aerospace applications. IFAC Proc. Vol. 35, 67–78. https://doi.org/10.3182/20020721-6-ES-1901.01237.

He, L., Ma, W., Guo, P., Sheng, T., 2021. Developments of attitude determination and control system of microsats: A survey. Proc. Institut. Mech. Engineers, Part I: J. Syst. Control Eng. 235 (10), 1733–1750. https://doi.org/10.1177/095965181989517.

Ismail, Z., Varatharajoo, R., 2020. A fractional-order sliding mode control for nominal and underactuated satellite attitude controls. Adv. Space Res. 66, 321–334. https://doi.org/10.1016/j.asr.2020.02.022.

Kim, S.W., Park, S.Y., Park, C., 2016. Spacecraft attitude control using neuro-fuzzy approximation of the optimal controllers. Adv. Space Res. 57 (1), 137–152. https://doi.org/10.1016/j.asr.2015.09.016.

Kuo, Y., Resmi, I.E.C., 2019. Model predictive control based on a Takagi-Sugeno fuzzy model for nonlinear systems. Int. J. Fuzzy Syst. 21, 556–570.

Liop, J.V., Polat, H.C., Romano, M., 2019. Attitude stabilization of spacecraft in very low earth orbit by center-of-mass shifting. Front. Robot. AI. https://doi.org/10.3389/frobt.2019.00007.

Nova, M., Carpintero, D.M., Saez, D., 2022. Fuzzy model predictive control for Takagi & Sugeno systems with optimised prediction dynamics. In: European Control Conference, UK. https://doi.org/10.23919/ECC55457.2022.9838066.

O'Dea, S., Burdick, P., Downer, J., Eisenhaure, D., Larkin, L., 1985. Design and development of a high efficiency effector for the control of attitude and power in space systems. 20th Proceedings of Intersociety Energy Conversion Engineering Conference, Warrandale.

Richie, D.J., Tsiotras, P., Fausz, J.L., 2001. Simultaneous attitude control and energy storage using VSCMGs: Theory and simulation. In: Proceedings of the 2001 American Control Conference, Arlington, VA, USA, pp. 3973–3979. https://doi.org/10.1109/ACC.2001.946291.

Roithmayr, C.M., 1999. International space station attitude control and energy storage experiment: effects of flywheel torque. NASA Tech. Memo., 209100

Rouyan, N., Chak, Y.-C., Varatharajoo, R., 2019. A feasibility review of SMC-MIMO based control architecture for high angle of attack flight.

Int. J. Multiphys. 13, 339–350. https://doi.org/10.21152/1750-9548.13.4.339.

Sarwar, S., Aslam, S., Haider, F., et al., 2019. Computational comparison between MPC and SR-MPC for fast dynamic system in presence of hard constraints. In: Proceedings of 4th International Conference on Emerging Trends in Engineering, Sciences and Technology, Karachi, Pakistan. https://doi.org/10.1109/ICEEST48626.2019.8981697.

Sivaprakash, N., Shanmugam, J., 2005. Neural network based three axis satellite attitude control using only magnetic torquers. 24th Digital Avionics Systems Conference, vol. 2. IEEE, p. 6-pp. https://doi.org/10.1109/DASC.2005.1563440.

Toth, R., Felici, F., Heuberger, P.S.C., Van Den Hof, P.M.J., 2008. Crucial aspects of zero-order hold LPV state-space system discretization. In: Proceedings of the 17th World Congress. The International Federation of Automatic Control, Korea. https://doi.org/10.3182/20080706-5-KR-1001.00832.

Tsiotras, P., Shen, H., Shen, C., 2001. Satellite attitude control and power tracking with energy/momentum wheels. J. Guid. Control Dyn. 24, 23–34. https://doi.org/10.2514/2.4705.

Varatharajoo, R., 2004. A combined energy and attitude control system for small satellites. Acta Astronaut. 54 (10), 701–712. https://doi.org/10.1016/j.actaastro.2003.12.004.

Varatharajoo, R., 2006a. Onboard errors of the combined energy and attitude control system. Acta Astronaut. 58 (11), 561–563. https://doi.org/10.1016/j.actaastro.2006.01.011.

Varatharajoo, R., 2006b. Operation for the combined energy and attitude control system. Aircr. Eng. Aerosp. Technol. 78 (6), 495–501. https://doi.org/10.1108/00022660610707166.

Varatharajoo, R., Fasoulas, S., 2002. Methodology for the development of combined energy and attitude control systems for satellites. Aerosp. Sci. Technol. 6 (4), 303–311. https://doi.org/10.1016/S1270-9638(02)01157-4.

Varatharajoo, R., Wooi, C.T., Mailah, M., 2011. Attitude pointing enhancement for combined energy and attitude control system. Acta Astronaut. 68 (11–12), 2025–2028. https://doi.org/10.1016/j.actaastro.2010.11.006.

Wang, L., 2004. A tutorial on model predictive control: using a linear velocity-form model. Dev. Chem. Eng. Mineral Process. 12 (5/6), 573–614.

Wang, L., 2009. Model Predictive Control System Design and Implementation Using MATLAB. Springer.

Wang, Y., Zou, L., Ma, L., Zhao, Z., Guo, J., 2021. A survey on control for Takagi-Sugeno fuzzy systems subject to engineering-oriented complexities. Syst. Sci. Control Eng. 9 (1), 334–349.

Yoon, H., Tsiotras, P., 2002. Spacecraft adaptive attitude and power tracking with variable speed control moment gyroscopes. J. Guid. Control Dyn 25, 328–342. https://doi.org/10.2514/2.4987.

Zagorski, P., 2012. Modeling Disturbances Influencing an Earth-orbiting Satellite. Pomiary Automatyka Robotyka.